

# Harnessing Interpretable and Unsupervised Machine Learning to Address Big Data from Modern X-ray Diffraction

Jordan Venderley<sup>1</sup>, Michael Matty<sup>1</sup>, Matthew Krogstad<sup>2</sup>, Jacob Ruff<sup>3</sup>,  
Geoff Pleiss<sup>4</sup>, Varsha Kishore<sup>4</sup>, David Mandrus<sup>5</sup>, Daniel Phelan<sup>2</sup>,  
Lekh Poudel<sup>6,7</sup>, Andrew Gordon Wilson<sup>8</sup>, Kilian Weinberger<sup>4</sup>,  
Puspa Upreti<sup>2,9</sup>, Stephan Rosenkranz<sup>2</sup>, Raymond Osborn<sup>2</sup>, Eun-Ah Kim<sup>1\*</sup>

<sup>1</sup>Department of Physics, Cornell University

<sup>2</sup>Materials Science Division, Argonne National Laboratory

<sup>3</sup>Cornell High Energy Synchrotron Source, Cornell University

<sup>4</sup>Department of Computer Science, Cornell University

<sup>5</sup>Department of Materials Science and Engineering, University of Tennessee

<sup>6</sup>Department of Materials Science and Engineering, University of Maryland

<sup>7</sup>NIST Center for Neutron Research, National Institute of Standard and Technology

<sup>8</sup>Courant Institute of Mathematical Sciences, New York University

<sup>9</sup>Department of Physics, Northern Illinois University

\*To whom correspondence should be addressed; E-mail: eun-ah.kim@cornell.edu.

**The information content of crystalline materials becomes astronomical when distortions, defects, phase heterogeneity, and collective electronic behavior are taken into account. In the past decade, improvements in source brightness and detector technology at modern x-ray facilities have allowed a dramatically increased fraction of this information to be captured. Now, the primary challenge is to understand and discover scientific principles from big data sets when a comprehensive analysis is beyond human reach. We report the development of a novel unsupervised machine learning approach, *XRD Temperature***

*Clustering (X-TEC)*, that can automatically extract charge density wave (CDW) order parameters and detect intra-unit cell (IUC) ordering and its fluctuations from a series of high-volume X-ray diffraction (XRD) measurements taken at multiple temperatures. We apply *X-TEC* to XRD data on a quasi-skutterudite family of materials,  $(\text{Ca}_x\text{Sr}_{1-x})_3\text{Rh}_4\text{Sn}_{13}$ , to obtain a quantum phase diagram as charge density wave order gets suppressed with doping. We further apply *X-TEC* to XRD data on a pyrochlore superconductor that undergoes multiple structural phase transitions,  $\text{Cd}_2\text{Re}_2\text{O}_7$ , to investigate the nature of the ordered phases under debate and their associated IUC distortions as well as order parameter fluctuations. Our approach can radically transform XRD experiments by allowing in-operando data analysis and enabling researchers to refine experiments by discovering interesting regions of phase space on-the-fly.

[1] From the early days of X-ray diffraction (XRD) experiments, they have been used to access atomic scale information in crystalline materials. The primary challenge has always been how to interpret the angle dependent scattering intensities of the resultant diffraction patterns (Fig 1(a)). Bragg and Bragg's initial insights into how to interpret such data (1) enabled the direct determination of crystal structures for the first time, and they were duly awarded a Nobel prize. Since the phase of the X-ray photon is lost in the measurement, the most common approach to interpreting XRD data is to employ forward modeling using the increasingly sophisticated tools of crystallography developed over the past century. These have been remarkably successful in determining the structure of highly crystalline materials, from simple inorganic solids to complex protein crystals. However, subtle structural changes can be difficult to determine when they only result in marginal changes in intensities without any change in peak locations (2). Furthermore, thermal and quantum fluctuations captured in diffuse scattering away from the Bragg peaks are beyond the reach of conventional crystallographic analysis. The

information-rich diffuse scattering is typically weaker than Bragg scattering by several orders of magnitude and can be difficult to differentiate from background noise.

[2] The massive data that modern facilities generate, spanning 3D reciprocal space volumes that include  $\mathcal{O}(10^4)$  Brillouin zones (BZ) (Fig 1(a-b)), at rates of  $\mathcal{O}(10^2)$  gigabytes per hour are sufficient to reveal the systematics of such subtle atomic scale information. Yet the sheer quantity of data presents a major challenge because collective phenomena take up only a tiny fraction of the total volume, making a manual search of the data an impossible task. Overcoming this challenge is of paramount importance especially in searching for an unknown order parameter. Specifically, two types of collective emergent phenomena are targets of XRD (see Figs. 1(c-e)). The first type results in an increase in the unit-cell size, for example due to charge density wave (CDW) formation. Compared to the structure at high temperature (Fig. 1c), a CDW results in new super-lattice peaks at  $Q = 2\pi/\lambda$  for a CDW with wavelength  $\lambda$  in a one-dimensional system, below the critical temperature  $T_c$  (Fig. 1d). While this is trivial to see in a one-dimensional system, searching for the emergence of new peaks in 3D reciprocal space with  $\mathcal{O}(10^4)$  Brillouin zones (BZ) is a challenging task. Moreover, weak and fluctuating signals have often required a targeted search (3, 4). The second type results in intra-unit cell (IUC) distortions due to a change in crystal symmetry without a change in the unit-cell volume (Fig 1(e)), which presents different challenges. IUC order generally leads to subtle changes in the structure factors of Bragg peaks (5) rather than the appearance of new peaks, unless there are changes in extinction rules. Nevertheless, IUC distortions are becoming important scientific objectives, with electronic nematic order increasingly recognized in diverse physical systems (6, 7) and its discovery requiring new approaches (8, 9).

[3] To extract atomic scale information encoded in massive XRD data volumes, we have developed *X-TEC*, a novel unsupervised machine learning approach that can discover the two collective phenomena of interest: a CDW transition and an IUC distortion. Machine learning is

increasingly employed for the analysis of complex experimental data (10–15) with an emphasis on supervised learning using hypothesis-driven synthetic data (10–12). However, the purpose of scientific discovery in experimental data would benefit enormously from an interpretable and unsupervised approach that does not rely on system-specific assumptions. Our methodology follows from the fundamental principle that a change in the collective state of a system occurs in the direction of minimizing the Helmholtz free energy  $F$ :

$$F = E - TS, \quad (1)$$

where  $E$  stands for the internal energy determined by the Hamiltonian for the system,  $T$  represents the temperature, and  $S$  represents the entropy. When the temperature  $T$  is lowered below a certain threshold, the entropy  $S$  gives way to the ordered state dominated by the system Hamiltonian. Hence it should be possible to zoom into the reciprocal space points that represent collective phenomena by tracking how the XRD intensity for each  $\vec{q}$ ,  $I(\vec{q}, T)$ , evolves with a change in temperature  $T$ . Inspired by high-dimensional clustering approaches that learn qualitative differences in the voice trains for speaker verification (16) (see Fig.1(f)), *X-TEC* discovers an ordering phenomena by clustering the “temperature-series” associated with given  $\vec{q}$ ,  $I(\vec{q}, T)$ , according to qualitative features in the temperature dependence, even when the raw temperature-series is massive and chaotic to human eyes (see Fig.1(g)).

[4] Fig 2 illustrates the steps of the *X-TEC* pipeline benchmarked on the well-known CDW material  $\text{TiSe}_2$  (17, 18). *X-TEC* starts by collecting XRD data on a single crystal encompassing many Brillouin zones in reciprocal space over a range of temperatures  $\{T_1, \dots, T_{dT}\}$  (see Fig 2a). The data is then put through a two-stage preprocessing to deal with two key challenges against working with comprehensive data: the volume and the dynamic range of the intensity scale. First, we threshold our data in order to simultaneously reduce its size and isolate its meaningful features. The volume is set by the  $\sim 10^9$  grid points in 3D reciprocal space

grid  $\{\vec{q} = (q_x, q_y, q_z)\}$  for a single temperature and the 10-30 temperatures measurements typically collected. However, the relevant peaks are sparse in  $\vec{q}$ -space for crystalline samples. We thus developed an automated thresholding algorithm (SM section IIa) which removes low intensity noise and reduces the number of  $\vec{q}$ -space points to be canvassed from the full grid to a selection of points  $\{\vec{q}_i\}$ , see Fig. 2b. Second, we rescale the remaining temperature series  $\{I(\vec{q}_i, T_j), j = 1, \dots, d^T\}$  still exhibiting a formidable dynamic range (see Fig 2d) in order to compare trajectories at different intensities scales, focusing on their temperature dependence rather than the absolute scale. For this, each trajectory is assigned a z-score (divided by standard deviation after its average value is subtracted). With some datasets, we find it useful to employ an alternative rescaling scheme that facilitates further variance-based thresholding as described in the supplementary materials (see SM section IIa).

[5] We now cluster the resulting collection of preprocessed temperature trajectories,  $\tilde{\mathbf{I}}(\vec{q}_i) \equiv \{\tilde{I}(\vec{q}_i, T_j); j = 1, \dots, d^T\}$  for each  $\vec{q}_i$  to discover qualitatively distinct types of temperature dependences in the data. For this, we adopt a Gaussian mixture model (GMM) (19). Our approach is to initially ignore correlations between different reciprocal space points ( $\vec{q}$ 's) and treat each temperature series  $\tilde{\mathbf{I}}(\vec{q}_i)$  as an independent point in the  $d^T$  dimensional Euclidean space  $\mathbf{R}^{d^T}$ . The GMM assumes that each point in the data set  $\{\tilde{\mathbf{I}}(\vec{q}_i)\}$  has been independently and identically generated by a weighted sum of  $K$  distinct multivariate normal distributions. The number of clusters,  $K$ , is the only parameter we set manually. The hyperparameters to be learned are the mixing weights  $\pi_k$ ,  $d^T$ -dimensional means  $\mathbf{m}_k$ ,  $d^T \times d^T$ -dimensional covariances  $\mathbf{s}_k$ ,  $(\pi, \mathbf{m}, \mathbf{s}) \equiv \{(\pi_k, \mathbf{m}_k, \mathbf{s}_k); k = 1, \dots, K\}$ . The associated model log-likelihood is

$$\log p(\{\tilde{\mathbf{I}}(\vec{q}_i)\} | \pi, \mathbf{m}, \mathbf{s}) = \sum_{\vec{q}_i} \log \left[ \sum_{k=1}^K \pi_k \mathcal{N}(\tilde{\mathbf{I}}(\vec{q}_i) | \mathbf{m}_k, \mathbf{s}_k) \right], \quad (2)$$

Here,  $\mathcal{N}(\tilde{\mathbf{I}}(\vec{q}_i) | \mathbf{m}_k, \mathbf{s}_k)$  is the probability density for the  $k^{th}$  multivariate Gaussian with mean

$\mathbf{m}_k$  and covariance  $\mathbf{s}_k$  evaluated at  $\tilde{\mathbf{I}}(\vec{q}_i)$ , i.e.,

$$\mathcal{N}(\tilde{\mathbf{I}}(\vec{q}_i)|\mathbf{m}_k, \mathbf{s}_k) \equiv \frac{1}{(2\pi)^{d_T/2}} \frac{1}{\sqrt{\det \mathbf{s}_k}} e^{-\frac{1}{2} [\tilde{\mathbf{I}}(\vec{q}_i - \mathbf{m}_k)^\dagger \mathbf{s}_k^{-1} (\tilde{\mathbf{I}}(\vec{q}_i) - \mu_k)]}. \quad (3)$$

The probability,  $w_i^k$ , that the temperature series labeled by  $\vec{q}_i$  belongs to the  $k^{th}$  cluster is

$$w_i^k = \frac{\pi_k \mathcal{N}(\tilde{\mathbf{I}}(\vec{q}_i)|\mathbf{m}_k, \mathbf{s}_k)}{\sum_k \pi_k \mathcal{N}(\tilde{\mathbf{I}}(\vec{q}_i)|\mathbf{m}_k, \mathbf{s}_k)}, \quad (4)$$

according to Bayes' theorem (see SM section IIc). We fix the hyper-parameters  $(\pi, \mathbf{m}, \mathbf{s})$  using a stepwise expectation maximization (EM) algorithm (20). Much like mean-field theory familiar to physicists, the EM algorithm iteratively searches for the saddle point of the lower bound of the log-likelihood

$$\tilde{\ell}(\{w_i^k, \pi_k, \mathbf{m}_k, \mathbf{s}_k\}) = \sum_{i,k} w_i^k \log \left[ \frac{\pi_k \mathcal{N}(\tilde{\mathbf{I}}(\vec{q}_i)|\mathbf{m}_k, \mathbf{s}_k)}{w_i^k} \right] + \lambda(1 - \sum_k \pi_k), \quad (5)$$

where  $\lambda$  is a Lagrange multiplier. The cluster assignment of the given reciprocal space point  $\vec{q}_i$  is then determined by the converged value of the clustering expectation  $\arg \max_k \{w_i^k\}$ .

[6] Fig 2e shows the outcome of the *X-TEC* applied to XRD data of bulk 1T-TiSe<sub>2</sub>, collected at the Cornell High Energy Synchrotron Source (CHESS). As a test case, we specifically explored non-Bragg trajectories associated with a  $3 \times 3 \times 3$  set of BZs, with the number of clusters set to  $K = 2$ . The contrast between the means of the magenta cluster and the teal cluster makes it evident that the magenta cluster represents the order parameter and the temperature at which it crashes down is the critical temperature. The separation between the means exceeding the individual variance affirms the clustering to be a meaningful result. Interpretation of the *X-TEC* results is immediate upon locating the two clusters in reciprocal space, as shown in Fig 2c, and inspecting the raw data. The location of the magenta cluster identifies the CDW wave vector to be  $\vec{Q}_{CDW} = \{(\pi, 0, \pi), (\pi, \pi, \pi)\}$ , and equivalent momenta in the hexagonal basis. *X-TEC* thus detected the CDW transition with the correct transition temperature  $T_c = 200$  K and correct ordering wavevector  $\vec{Q}_{CDW}$  (21) without any prior knowledge.

[7] Now we turn to new high volume XRD data on a CDW material family with a putative quantum critical point:  $(\text{Ca}_x\text{Sr}_{1-x})_3\text{Rh}_4\text{Sn}_{13}$ , a quasi-skutterudite family (see Fig. 3a). Electrical resistivity and heat capacity experiments on this material family indicated a potential quantum critical point at a composition of  $x = 0.9$  under ambient pressure (see Fig 3f) (22). Although there have been extensive theoretical and experimental studies of quantum phase transitions associated with spin density wave and nematic ordering (23–26), relatively little is known about quantum phase transitions associated with charge density wave ordering (27–29).  $(\text{Ca}_x\text{Sr}_{1-x})_3\text{Rh}_4\text{Sn}_{13}$  and related compounds have therefore attracted considerable interest concerning the relationship between quantum fluctuations originating from structural instabilities and superconductivity (30–32). Here we apply *X-TEC* to around 200 GB of XRD data on four compounds, ( $x = 0, 0.1, 0.6, 0.65$ ) and map out the phase diagram as a function of temperature and doping with no prior knowledge regarding the order parameter given to *X-TEC*.

[8]The x-ray measurements on  $(\text{Ca}_x\text{Sr}_{1-x})_3\text{Rh}_4\text{Sn}_{13}$  were taken on Sector 6-ID-D at the Advanced Photon Source using a monochromatic x-ray energy of 87 keV. Images are collected on a fast area detector (Pilatus 2M CdTe) at a frame rate of 10 Hz while the sample is continuously rotated through  $360^\circ$  at a speed of  $1^\circ$  per second (Fig. 1a). These rotation scans are repeated twice to fill in gaps between the detector chips, so a single measurement represents an uncompressed data volume of over 100 GB collected in 20 minutes. This allows comprehensive measurements of the temperature dependence of a material in much less than a day. Using a cryostream, we are able to vary the temperature from 30 K to 300 K. The rotation scans sweep through a large volume of reciprocal space (Fig. 1a); when the data are transformed into reciprocal space coordinates, the 3D arrays are typically reduced in size by an order of magnitude. More details of both the measurement and data reduction workflow are given in Ref. 33, see also SM I.

[9] *X-TEC* in its simplest form as described in Fig 2, assumes that each temperature series

$\tilde{\mathbf{I}}(\vec{q}_i)$  is independent. However, there are clearly correlations in our data. Specifically, we anticipate correlations among nearby momenta since experiments are resolution limited and intensity peaks in reciprocal space are broadened by fluctuations and noise. We also expect periodic zone-to-zone correlations. Since ignoring these correlations can lead to spurious results, we incorporate these correlations using label smoothing (see SM section IIb) similar to how signals from different cameras can be correlated for computer vision (34) (Fig. 3b). Label smoothing corrects the independence assumption and enforces local smoothness across the cluster assignments of points with similar momenta within and across Brillouin zones. The algorithm first constructs a nearest neighbor graph in momentum space, connecting reciprocal space points that share similar momenta. For each point, the neighbors are weighted by their distance in momentum space and the weights normalized. Label smoothing averages the cluster assignments of a point with its (weighted) neighbors. We incorporate this smoothing step between the E- and M- step of the GMM. In Figs. 3c and 3d, we present the two-cluster ( $K = 2$ ) clustering results for undoped  $\text{Sr}_3\text{Rh}_4\text{Sn}_{13}$  with and without label smoothing respectively. The identification of CDW ordering at  $q_{CDW} = (0.5, 0.5, 0)$  and symmetry equivalents with respect to the cubic Bragg peaks is robust in both figures. The outcome of *X-TEC* points to a CDW transition temperature of  $T_c \approx 130$  K for this material. However, label smoothing eliminates the unphysical intra-peak cluster separation present in Fig 3c.

[10] Plotting the CDW order parameters extracted at each doping, we can track the evolution of the critical temperature  $T_c$  as a function of chemical pressure (fig 3e). The critical temperatures may be extracted by fitting the data to the functional form  $\alpha(T_c - T)^{2\beta}$ . We've marked our critical points on top of the phase diagram provided in (35) (fig 3f) and find good agreement with previously reported results (31). The critical exponent,  $\beta$ , derived from the temperature dependence of the ML clusters, falls from 0.49 at  $x = 0$  to 0.25 at  $x = 0.1$ , but unfortunately we have too small a temperature range to determine  $\beta$  reliably at higher  $x$  close

to the quantum critical point. Nevertheless, instead of determining critical exponents by fitting a handful of peaks, *X-TEC* provides a means of including the entire data volume by clustering peak intensities from thousands of Brillouin zones to produce an analysis that is both robust and rapid in future studies of such phase diagrams.

[11] We now turn to the more challenging problem of detecting intra-unit cell order and order parameter fluctuations. The material system of choice is the first known pyrochlore superconductor  $\text{Cd}_2\text{Re}_2\text{O}_7$  (36–38) (see Fig. 4a), whose structural transitions and the nature of its low-temperature phases have recently attracted much interest (39–44).  $\text{Cd}_2\text{Re}_2\text{O}_7$  goes through a second-order transition at  $T_{s1} = 200$  K with clear thermodynamic signatures (see Fig. 4b), from the cubic pyrochlore  $Fd\bar{3}m$  structure (phase I) to a structure that breaks inversion symmetry. There are eight possible inversion-breaking space groups that can be accessed by a second-order transition (45), but the correct structure of the phase for  $T < T_{s1}$  (phase II) is still debated (39, 46). Moreover, the structures below a first-order transition at  $T_{s2} = 113$  K (phase III) and below a recently posited additional transition at 80 K are poorly understood (41). A combination of small atomic displacements with crystallographic twinning (47) has made it challenging to determine the structure of these low symmetry states using traditional crystallographic approaches (48, 49). Previous XRD results for phase II are consistent with two nearly-degenerate and independent space groups  $I\bar{4}m2$  and  $I4_122$  which form two components of the  $E_u$  order parameter, a rank-2 tensor. This degeneracy, which is protected by the point group symmetry of phase I (45), requires a gapless collective excitation, a Goldstone mode (50, 51). While Raman scattering (52) and non-linear optical studies (53) found evidence of the Goldstone phonon mode in phase II and phase III, confirmation of such fluctuations has been beyond the reach of XRD. Moreover, a recent non-linear optical study raised the possibility that the  $E_u$  order parameter is secondary to a  $T_{2u}$  primary order parameter of electronic origin (46). This implied that any structural signature of the newly proposed primary order parameter had been

missed by previous XRD measurements (47, 48). Furthermore, information that goes beyond identifying the structural space groups, i.e., concerning the atomic displacements themselves, has been out of experimental reach thus far.

[12] We performed x-ray scattering measurements over a wide temperature range ( $30\text{ K} < T < 300\text{ K}$ ) on a single crystal of  $\text{Cd}_2\text{Re}_2\text{O}_7$ , which our measurements show is untwinned, at least in the Phase II. This may be due to the small volume ( $400 \times 200 \times 50\text{ }\mu\text{m}^3$ ) required for our synchrotron measurements. We first performed scans using an x-ray energy of 87 keV, which contained scattering spanning nearly 15,000 Brillouin zones, in order to search for previously undetected peaks and determine the systematic ( $HKL$ ) dependence of the Bragg peak intensities at each temperature. To better understand order parameter fluctuations, we then reduced the energy to 60 keV to improve the  $\vec{Q}$ -resolution and increased the number of temperatures, particularly near the phase transitions. We comprehensively analyzed the resulting data sets with a combined volume of nearly 8 TB using *X-TEC*.

[13] A first pass of *X-TEC* with a simple form of label smoothing<sup>1</sup> for two clusters ( $K = 2$ ) readily finds a cluster whose intensity rises sharply at  $T_{s1} = 200\text{ K}$  (see the purple cluster in Fig. 4c). The crisp clustering results with tight variance around the means reflect amplification of the meaningful trend upon using data from a large number of BZ's. By examining the *X-TEC* cluster assignments, we find the purple cluster to exclusively consist of peaks with  $\vec{Q} = (H, K, L)$ , with all indices even, exactly one of which is not divisible by four, using the cubic indices of Phase I (see Fig. 4d). Peaks that are equivalent in the cubic phase have different temperature dependence in Phase II, implying that the sample is untwinned, something that is confirmed by our high-resolution data. This means that the presence of  $(00L)$  peaks with  $L = 4n + 2$  below  $T_{s1}$  in phase II unambiguously rules out all the tetragonal space groups compatible with the pyrochlore structure, apart from  $I\bar{4}m2$  and  $I\bar{4}$ . According to an earlier group theoretical

---

<sup>1</sup>Here we simply averaged peaks due to the volume of the data.

analysis (45), of these two, only the former is compatible with a single second-order phase transition, so our data is strong confirmation of previous conclusions that, at  $T_{s1}$ , an  $E_u$  mode condenses to produce an  $I\bar{4}m2$  phase (49, 53).

[14] This only defines the phase II space group, not the intra-unit cell distortions (*cf* Fig. 1e). To throw light on the relative atomic displacements, we have applied *X-TEC* to the high-resolution data, identifying four clusters with distinct temperature dependences ( $K = 4$ ) (See SM section IIIa). This reveals that there are four sub-clusters; the cubic-forbidden peaks (purple in Fig. 4c,d) are divided into two of them, while the cubic-allowed peaks (yellow in Fig. 4c,d) contribute to all four. The temperature dependence of the four clusters strikingly reveals the first-order character of the  $T_{s2}$  transition, with sudden jumps in all the peak intensities that have not been seen so clearly before, although there are hints in earlier x-ray data (48). Fig. 4e shows the temperature dependence of the two sub-clusters (red and blue) of cubic-forbidden peaks and their fits, in which we treat the displacements as order parameters with a common exponent  $\beta$  (see SM IIIc). The red cluster shows a sharp increase in intensity at  $T_{s2}$ , while the blue cluster shows a sudden drop. The  $(HKL)$  assignments show that the two clusters correspond to two distinct classes of structure factor, whose values only depend on the distortions of the Cd and Re sublattices: the red cluster consists of peaks that are dominated by  $z$ -axis displacements,  $(\delta z_{Cd}, \delta z_{Re})$  and those in the blue cluster by in-plane displacements, along  $x$  or  $y$  depending on the Wyckoff position,  $(\delta x_{Cd}, \delta x_{Re})$  (SM IIIb). We can draw two conclusions from these and other fits. First, peaks in all four clusters (*i.e.*, all the measured Bragg peaks) are consistent with a common exponent of  $\beta \approx 0.25$  close to  $T_{s1}$ . This is close to the value expected for a 2D-XY system (54). It also confirms that the  $E_u$  order parameter is primary, contrary to the conclusions of ref. (46). Furthermore, the flat temperature dependence of the red cluster below 180 K results from out-of-phase distortions of the Cd and Re sublattices. The refined values of  $(\delta z_{Cd}$  and  $\delta z_{Re})$  are approximately equal and opposite (see Fig. 4f). This is a remarkable example

where the temperature dependence of order parameters constrains the relative internal displacements in a way that has eluded conventional structural refinement, although it is not possible to determine their absolute magnitude. The fact that there is no corresponding flattening of the blue cluster indicates that the in-plane displacements are either in phase or are dominated by one or other cations. Finally, the abrupt increase in the red cluster intensity at  $T_{s2} = 113$  K signals the disappearance of this out-of-phase relation upon the first order transition into phase III, suggesting a sudden reorientation of the internal distortions.

[15] We now seek information on the order parameter fluctuations. In peak average analysis of Fig. 4c-e, the center of the peak dominates the analysis, while any evidence of fluctuation should be in the diffuse scattering around the Bragg peaks. Accordingly, we now analyze all  $\tilde{I}(\vec{q}_i, T)$  of the high-resolution data independently, restricting the temperature range to  $T < 160$  K to avoid the effect of critical fluctuations. The cluster means of four-cluster *X-TEC* are shown in the inset of Fig. 4g.<sup>2</sup> The reciprocal space distribution of the clusters reveals a striking observation. While all the peak centers form a single cluster with relatively mild temperature dependence at these temperatures (shown in black in Fig. 4g), the halo of diffuse scattering fall into one of two separate clusters, shown in red and blue in Fig. 4g. The cluster means in the inset indicate the red halo sustains intensity throughout Phase II to only dive down at  $T_{s2} = 113$  K while the blue halo picks up intensity at around  $T_{s2}$  to abruptly die out at around 90 K. The temperature evolution of representative line cuts shown at the bottom of Fig. 4g confirms these observations in the data. Together, these halos define fluctuations extending over the entire phase II and below that are supported by surprisingly broad regions around the Bragg peaks. This is clearly distinct from critical fluctuations, which peak close to  $T_{s1}$  (see SM section IIId) but is entirely consistent with the Goldstone modes observed in Raman scattering (52). Furthermore, there is a one-to-one correspondence between the two clustering results shown

---

<sup>2</sup>We found no further gain of information for  $K > 4$ .

in Fig. 4e and Fig. 4g that reveals unprecedented microscopic detail of the Goldstone mode: substantial anti-phase  $\delta z$  fluctuations of the two cations dominate the fluctuations in the phase II, which gives way to in-plane fluctuations between  $90 \text{ K} < T < T_{s2}$ .

[16] Based on the *X-TEC* analysis, we conclude that  $\text{Cd}_2\text{Re}_2\text{O}_7$  orders at  $T_{s1}$  with a primary  $E_u$  order parameter exhibiting Goldstone mode fluctuations around the  $I\bar{4}m2$  phase, consistent with a two-component Mexican hat potential (51). We note that these represent fluctuations towards the second component of the  $E_u$  tensor, *i.e.*, with  $I4_122$  symmetry, in which the in-plane and  $z$ -axis displacements revert to their cubic values, so it is natural for there to be a strong correlation between the structure factors and the associated fluctuations around each Bragg peak, as indicated by the correspondence of the peak and diffuse scattering clusters. The sudden change in peak intensities at  $T_{s2}$  must result from a reorientation of the cation displacements. Below the transition, we still observe peaks that are forbidden by  $I4_122$  symmetry, even if the unique tetragonal axis has rotated. It is possible that this is due to the onset of twinning below  $T_{s2}$ , but it seems more likely that the symmetry transforms to  $F222$ , which is a linear combination of the two  $E_u$  components. We find no evidence of a well-defined phase transition at 80 K as proposed in recent Raman measurements (41), but the diffuse scattering does persist below  $T_{s2}$  and it is possible that there is a continuous adjustment of the cation displacements in the  $F222$  phase that lock in at the lower temperature.

[17] In summary, we developed *X-TEC*, an unsupervised and interpretable ML algorithm for voluminous XRD data that is guided by the fundamental role temperature plays in emergent phenomena. By analyzing the entire data set over many BZ's and making use of temperature evolutions, *X-TEC* can pick up subtle features representing both order parameters and fluctuations in those order parameters from higher intensity backgrounds. The algorithm is fast with  $O(10)$  minutes of run time for the tasks presented here. Using *X-TEC*, we obtained the quantum phase diagram for the CDW superconductor family  $(\text{Ca}_x\text{Sr}_{1-x})_3\text{Rh}_4\text{Sn}_{13}$ . In  $\text{Cd}_2\text{Re}_2\text{O}_7$ , we

conclusively identified the primary order parameter of the  $T_{s1} = 200$  K transition. We further revealed the nature of the intra-unit-cell atomic distortions in a way that has eluded crystallographic analysis until now. Finally, we revealed XRD evidence of a structural Goldstone mode for the first time. The unprecedented degree of microscopic information we have been able to unearth from the XRD is fitting for such comprehensive data but would have been impossible by manual inspection. Given the general structure of *X-TEC*, we anticipate it to be broadly applicable to other fields beyond XRD.

## References

1. W. H. Bragg, W. L. Bragg, *Proc. Roy. Soc. London. A* **88**, 428 (1913).
2. T. Egami, S. J. Billinge, *Underneath the Bragg peaks: structural analysis of complex materials* (Newnes, 2012).
3. P. Abbamonte, *et al.*, *Nature Physics* **1**, 155 (2005).
4. E. M. Forgan, *et al.*, *Nature Communications* **6**, 10064 (2015).
5. M. J. Lawler, *et al.*, *Nature* **466**, 347 (2010).
6. E. Fradkin, S. A. Kivelson, M. J. Lawler, J. P. Eisenstein, A. P. Mackenzie, *Ann. Rev. Cond. Matt.* **1**, 153 (2010).
7. R. M. Fernandes, P. P. Orth, J. Schmalian, *Ann. Rev. Cond. Matt.* **10**, 133 (2019).
8. J.-H. Chu, *et al.*, *Science* **329**, 824 (2010).
9. J.-H. Chu, H.-H. Kuo, J. G. Analytis, I. R. Fisher, *Science* **337**, 710 (2012).
10. Y. Zhang, *et al.*, *Nature* **570**, 484 (2019).

11. A. Bohrdt, *et al.*, *Nature Physics* **15**, 921 (2019).
12. S. Ghosh, *et al.*, *Science Advances* **6** (2020).
13. G. Torlai, *et al.*, *Phys. Rev. Lett.* **123**, 230504 (2019).
14. P. Ronhovde, *et al.*, *Scientific Reports* **2**, 329 (2012).
15. M. Ziatdinov, *et al.*, *npj Computational Materials* **6**, 21 (2020).
16. D. A. Reynolds, T. F. Quatieri, R. B. Dunn, *Digital signal processing* **10**, 19 (2000).
17. F. J. D. Salvo, D. E. Moncton, J. V. Waszczak, *Phys. Rev. B* **14**, 4321 (1976).
18. J. A. Wilson, A. D. Yoffe, *Adv. Phys.* **18**, 193 (1969).
19. K. P. Murphy, *Machine learning : a probabilistic perspective* (MIT Press, Cambridge, Mass. [u.a.], 2013).
20. P. Liang, D. Klein, *Proceedings of Human Language Technologies: The 2009 Annual Conference of the North American Chapter of the Association for Computational Linguistics, NAACL '09* (Association for Computational Linguistics, USA, 2009), pp. 611–619.
21. F. J. Di Salvo, D. E. Moncton, J. V. Waszczak, *Phys. Rev. B* **14**, 4321 (1976).
22. L. E. Klintberg, *et al.*, *Phys. Rev. Lett.* **109**, 237008 (2012).
23. T. Shibauchi, A. Carrington, Y. Matsuda, *Ann. Rev. Cond. Matt.* **5**, 113 (2014).
24. E. Berg, S. Lederer, Y. Schattner, S. Trebst, *Ann. Rev. Cond. Matt.* **10**, 63 (2019).
25. S. Sachdev, *Phys. Stat. Sol. B* **247**, 537 (2010).
26. R. Daou, *et al.*, *Nature Physics* **5**, 31 (2009).

27. E. Morosan, *et al.*, *Nature Physics* **2**, 544 (2006).
28. M. Monteverde, J. Lorenzana, P. Monceau, M. Nez-Regueiro, *Phys. Rev. B* **88**, 180504 (2013).
29. T. Gruner, *et al.*, *Nature Physics* **69**, 71 (2017).
30. W. C. Yu, *et al.*, *Phys. Rev. Lett.* **115**, 207003 (2015).
31. Y. W. Cheung, *et al.*, *Phys. Rev. B* **98**, 161103 (2018).
32. L. S. I. Veiga, *et al.*, *Phys. Rev. B* **101**, 104511 (2020).
33. M. J. Krogstad, *et al.*, *Nature Materials* **19**, 63 (2020).
34. Y. You, *et al.*, *8th International Conference on Learning Representations, ICLR 2020, Addis Ababa, Ethiopia, April 26-30, 2020* (OpenReview.net, 2020).
35. S. K. Goh, *et al.*, *Phys. Rev. Lett.* **114**, 097002 (2015).
36. R. Jin, *et al.*, *Phys. Rev. B* **64**, 180503 (2001).
37. M. Hanawa, *et al.*, *Phys. Rev. Lett.* **87**, 187001 (2001).
38. H. Sakai, *et al.*, *J. Phys. Cond. Matt.* **13**, L785 (2001).
39. Z. Hiroi, J.-i. Yamaura, T. C. Kobayashi, Y. Matsubayashi, D. Hirai, *J. Phys. Soc. Jpn* **87**, 024702 (2018).
40. M. R. Norman, *Phys. Rev. B* **101**, 045117 (2020).
41. K. J. Kapcia, *et al.*, *Phys. Rev. Research* **2**, 033108 (2020).
42. S. Di Matteo, M. R. Norman, *Phys. Rev. B* **96**, 115156 (2017).

43. Y. Matsubayashi, D. Hirai, M. Tokunaga, Z. Hiroi, *Journal of the Physical Society of Japan* **87**, 104604 (2018).
44. Y. Matsubayashi, *et al.*, *Phys. Rev. B* **101**, 205133 (2020).
45. I. A. Sergienko, S. H. Curnoe, *J. Phys. Soc. Jpn* **72**, 1607 (2003).
46. J. W. Harter, Z. Y. Zhao, J.-Q. Yan, D. G. Mandrus, D. Hsieh, *Science* **356**, 295 (2017).
47. J.-P. Castellan, *et al.*, *Phys. Rev. B* **66**, 134528 (2002).
48. J.-I. Yamaura, Z. Hiroi, *J. Phys. Soc. Jpn* **71**, 2598 (2002).
49. J.-i. Yamaura, *et al.*, *Phys. Rev. B* **95**, 020102 (2017).
50. J. Goldstone, A. Salam, S. Weinberg, *Phys. Rev.* **127**, 965 (1962).
51. Q. N. Meier, *et al.*, *Phys. Rev. B* **102**, 014102 (2020).
52. C. A. Kendziora, *et al.*, *Phys. Rev. Lett.* **95**, 125503 (2005).
53. J. C. Petersen, *et al.*, *Nature Physics* **2**, 605 (2006).
54. S. Bramwell, P. C. W. Holdsworth, *Journal of Physics: Condensed Matter* **5**, L53 (1993).
55. A. Ng, *CS229 Lecture notes* (2017).

## Acknowledgments

We acknowledge stimulating discussions with Michael Norman and the assistance of Anshul Kogar in the  $\text{TiSe}_2$  measurements. We thank Jeffrey Lynn and Johnpierre Paglione for assistance in preparing the  $(\text{Ca}_x\text{Sr}_{1-x})_3\text{Rh}_4\text{Sn}_{13}$  samples. Initial development of *X-TEC* (EAK, AW, KW, GP) was supported by NSF HDR-DIRSE award number OAC-1934714 and testing on  $\text{TiSe}_2$

data was supported by U.S. Department of Energy, Office of Basic Energy Sciences, Division of Materials Science and Engineering under Award DE-SC0018946 (JV). The experiments on  $(\text{Ca}_x\text{Sr}_{1-x})_3\text{Rh}_4\text{Sn}_{13}$  and  $\text{Cd}_2\text{Re}_2\text{O}_7$  (MK, SR, RO, PU, DP), and the subsequent machine learning analysis and theoretical interpretations of the results (EAK, VK, JV), were supported by the US DOE, Office of Science, Office of Basic Energy Sciences, Division of Material Sciences and Engineering. MM acknowledges support by the National Science Foundation (Platform for the Accelerated Realization, Analysis, and Discovery of Interface Materials (PARADIM)) under Cooperative Agreement No. DMR-1539918 and the Cornell Center for Materials Research with funding from the NSF MRSEC program (DMR-1719875). This research used resources of the Advanced Photon Source, a U.S. DOE Office of Science User Facility operated for the DOE Office of Science by Argonne National Laboratory under Contract No. DE-AC02-06CH11357. Research conducted at CHESS is supported by the National Science Foundation via Awards DMR-1332208 and DMR-1829070.

## Figure Captions

**Fig. 1** (a) Schematic geometry of the x-ray scattering measurements. A monochromatic x-ray beam is incident on the sample, which rotates about the orthogonal  $\phi$  axis while images are captured on a fast area detector. The reciprocal space map shows the  $\vec{q}$ -coverage of a single plane in the 3D volume after capturing images over a full  $360^\circ$  sample rotation. (b) Three-dimensional volume of reciprocal space covered by the x-ray scattering. Each red dot is a single Bragg peak. With an x-ray energy of 87 keV, a volume of over  $200 \text{ \AA}^3$  is measured, containing over ten thousand Brillouin zones if the unit cell dimension is  $10 \text{ \AA}$ . (c-e) Real space positions of atoms (top) and the corresponding scattering intensities (bottom) calculated from simulated one-dimensional crystals with a unit cell containing two atoms, illustrating (c) a high symmetry phase, with (d) distortions due to CDW order and (e) IUC order. In (c), the high symmetry phase produces peaks at integer  $\vec{q}$ . In (d), displacements of the orange atoms by  $\pm\delta$  double the size of the unit-cell producing additional super-lattice peaks at half-integer  $\vec{q}$  as well as changes in the other peak intensities. In (e), IUC distortions of the orange atoms by  $-\delta$  change the peak intensities without producing additional super-lattice peaks. (f) Sound waveform of two people simultaneously talking (left) can be separated through clustering represented by different color (right). (g) Example of raw intensity trajectories for  $\text{Sr}_3\text{Rh}_4\text{Sn}_{13}$ . The collection of individual raw temperature series  $I(\vec{q}_i, T)$  for each point  $\vec{q}_i$  in the entire data set.

**Fig. 2** (a) Two-dimensional slices of logged intensity,  $\log I(\vec{q}, T)$ , of  $1\text{T-TiSe}_2$  on the  $L = 3.5$  plane at three temperatures. This plane contains super-lattice peaks at  $T < T_c = 200\text{K}$  (left) that disappears with the melting of the CDW order (right). (b) Thresholding described in SM section IIa removes grey points from the reciprocal space of the plane shown in (a). Only the blue points belong to the set  $\{\vec{q}_i\}$  that is tracked using *X-TEC*. (c) Cluster assignments of  $\vec{q}_i$

in the  $L = 3.5$  plane. The magenta and teal points belong to the CDW cluster and the Background cluster respectively. **(d)** Raw intensity trajectories over  $d^T = 14$  temperature values,  $\{T_1 = 100K, \dots, T_{14} = 200K\}$ , of all  $\vec{q}_i$ -points in the 27 BZ's used for clustering. **(e)** Rescaled temperature series  $\tilde{I}(\vec{q}_i, T)$  from 27 Brillouin zones of  $\text{TiSe}_2$  (shown faintly) are clustered for two clusters ( $K = 2$ ). Solid lines denote cluster means  $\mathbf{m}$  for the non-trivial CDW cluster (magenta) and the background cluster (teal), interpolated between  $d^T = 14$  temperature points of measurement. Shading represents covariance (standard deviation)  $\mathbf{s}$ .

**Fig. 3** **(a)** Crystal structure of  $(\text{Ca}_x\text{Sr}_{1-x})_3\text{Rh}_4\text{Sn}_{13}$ . **(b)** Performing depth estimation for self driving cars, aggregating multiple sensor information with label propagation. Depth estimation from LIDAR (yellow) are highly accurate but sparse, while depth estimation from cameras (blue) are dense but noisy. Label propagation synthesizes the two sources, aligning the noisy camera observations to match LIDAR observations (34). **(c,d)** A comparison between two-cluster results of XRD data from  $(\text{Ca}_x\text{Sr}_{1-x})_3\text{Rh}_4\text{Sn}_{13}$  spanning approximately 50,000 BZ's (with the exact number for each sample being slightly different) with plain vanilla *X-TEC* treating all  $\vec{q}_i$ 's to be independent in (c) and employing label smoothing in (d). The upper panel of each figure shows the cluster means and variances interpolated between  $d^T = 24$  temperature points of measurement; the lower panel shows the corresponding cluster assignments of  $\vec{q}_i$  points that passed the thresholding in the  $q_l = 0$  plane. Nearby  $\vec{q}_i$  points are often assigned to different clusters without label smoothing. Label smoothing automatically harmonizes the assignments in the vicinity of each peaks at the cost of weakening the cluster separation. **(e)** The cluster means of the CDW clusters are interpolated and plotted to reveal order parameter like behavior for four samples at different values of Ca doping  $n$ . For these results, we use label smoothing and subtract the minimum from each cluster mean to aid in comparison. **(f)** The critical temperatures from the cluster means in (e) (magenta filled circles) overlaid onto

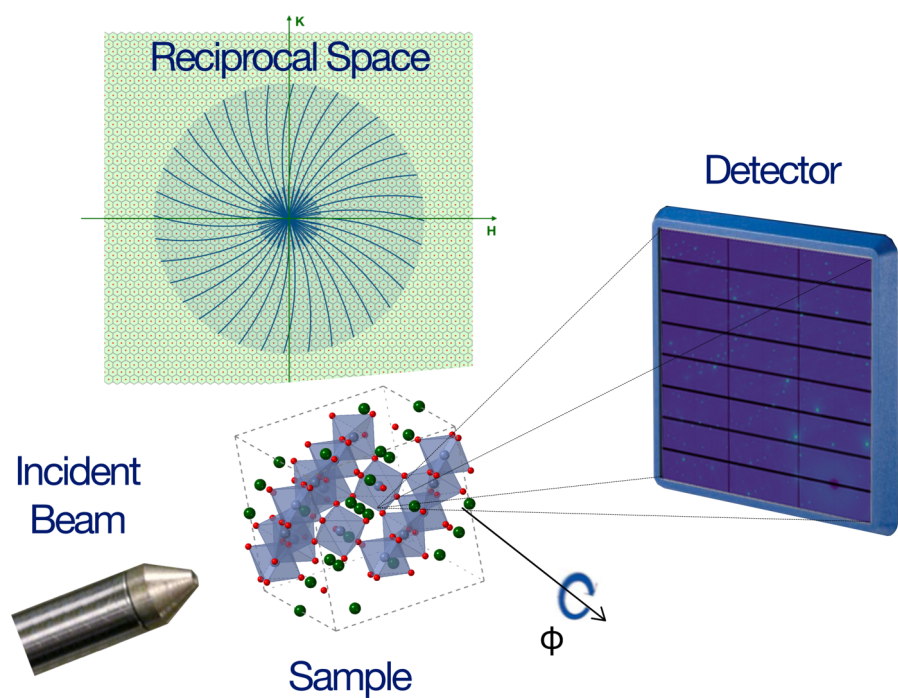
the known phase diagram from (35).

**Fig. 4** (a) Crystal structure of  $\text{Cd}_2\text{Re}_2\text{O}_7$ . (b) Temperature dependence of the specific heat of  $\text{Cd}_2\text{Re}_2\text{O}_7$ , showing the second-order phase transition at  $T_{s1}=200$  K and the first-order phase transition at  $T_{s2}=113$  K (see SM IIIa). Three temperature ranges are marked as phase I ( $T > T_{s1} = 200\text{K}$ ), phase II ( $T_{s2} = 113\text{K} < T < T_{s1}$ ), and phase III ( $T < T_{s2}$ ). (c) *X-TEC* results on the lower resolution data spanning 15,000 BZ's, clustered for two-clusters. Cluster means (solid lines) and standard deviations (shaded areas) for the two clusters are shown in purple and yellow, interpolated between  $d^T = 30$  temperature points of measurement. For this data set, the data are logged prior to the *X-TEC* preprocessing to suppress fluctuation signal and isolate the transition at  $T_{s2}$ . The notation  $\log(\widetilde{I}(\vec{q}_i, T))$  is denote that the data are logged before other preprocessing (see SM Section IIIb). (d) The cluster assignments of thresholded  $\vec{q}_i$  points in the  $H = 0$  plane that belong to the two clusters in (c) (see SM Section IIIb). (e) Four-cluster *X-TEC* results on the high resolution data is shown for the two sub-clusters that amount to cubic-forbidden peaks (the purple cluster in (c)). The cluster means are shown as red and blue solid points for each sub-cluster without interpolation. The solid lines are fit to these cluster means based on the model assuming  $\delta x$  displacements (blud) and  $\delta z$  displacements of cations to vary as  $(T - T_c)^\beta$ , with a common order parameter exponent of  $\beta = 0.25$  as discussed in SM Section IIIc. (f) Schematic diagram of the relative  $z$ -axis displacements of cation sublattices  $\delta z_{Cd}$  (red) and  $\delta z_{Re}$  (gray) with respect to the cubic phase, derived from the fits to the *X-TEC* cluster means shown in (e). The in-plane displacements are not shown for clarity. (g) The four-cluster ( $K=4$ ) cluster assignments of the high-resolution data for the  $\vec{q}_i$ -points in the  $H = 0$  plane, allowing all  $\vec{q}_i$  to behave independently. The inset shows the interpolated cluster means for  $d^T = 38$  temperature measurement points for ( $30 < T < 150$ ), away from the critical fluctuation associated with  $T_{s1}$ . The regions in the vicinity of two Bragg peaks at  $0\overline{4}6$  (left) and

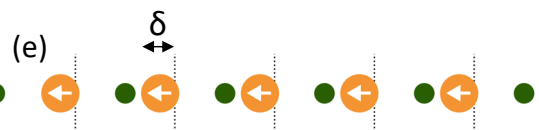
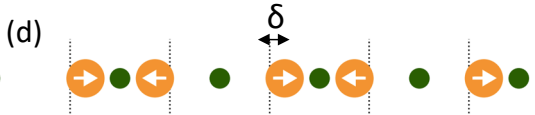
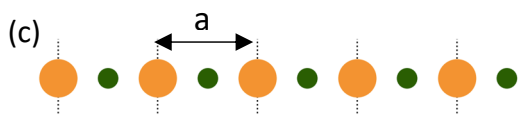
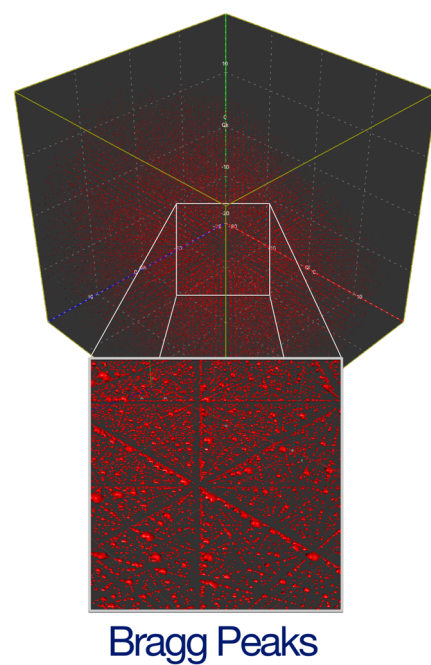
$0\bar{6}0$  (right) are magnified to show the peak centers in both belonging to the black cluster while halos form two distinct clusters separater from the center of the peaks, red and blue respectively. The raw intensity  $I(\vec{q}, T)$  plotted along a line cut for each of the peaks confirm the temperature dependence of the red halo intensities and the blue halo intensities represented by the cluster means in the inset. Specifically, the  $0\bar{4}\bar{6}$  peak has additional diffuse scattering above  $T_{s2} \approx 113$  K, consistent with the temperature dependence of the red cluster mean. The  $0\bar{6}0$  peak shows an anomaly near  $T_{s2}$  without additional diffuse scattering above, consistent with the temperature dependence of the blue cluster mean.

# Figure 1

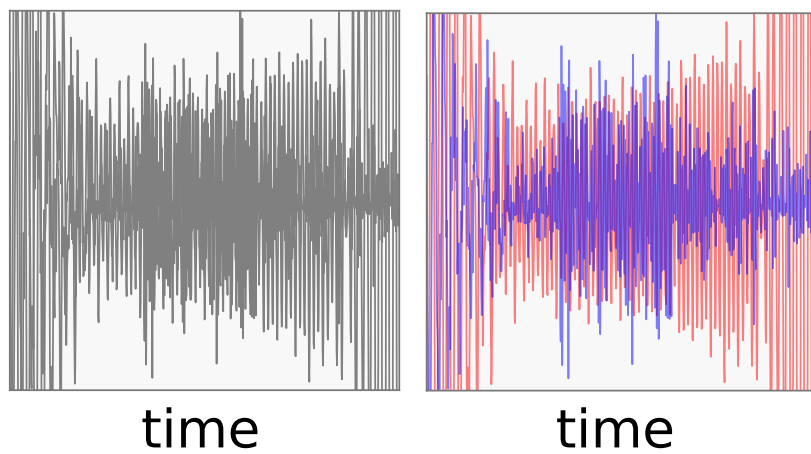
(a)



(b)



(f)



(g)

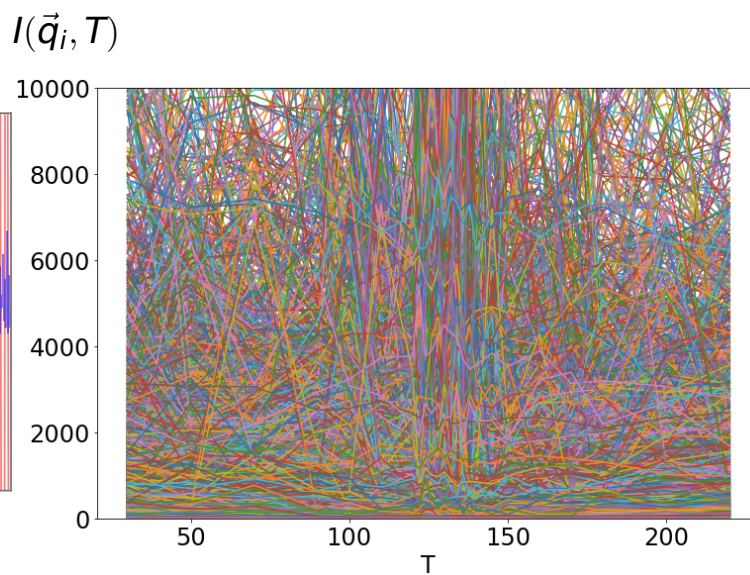


Figure 2

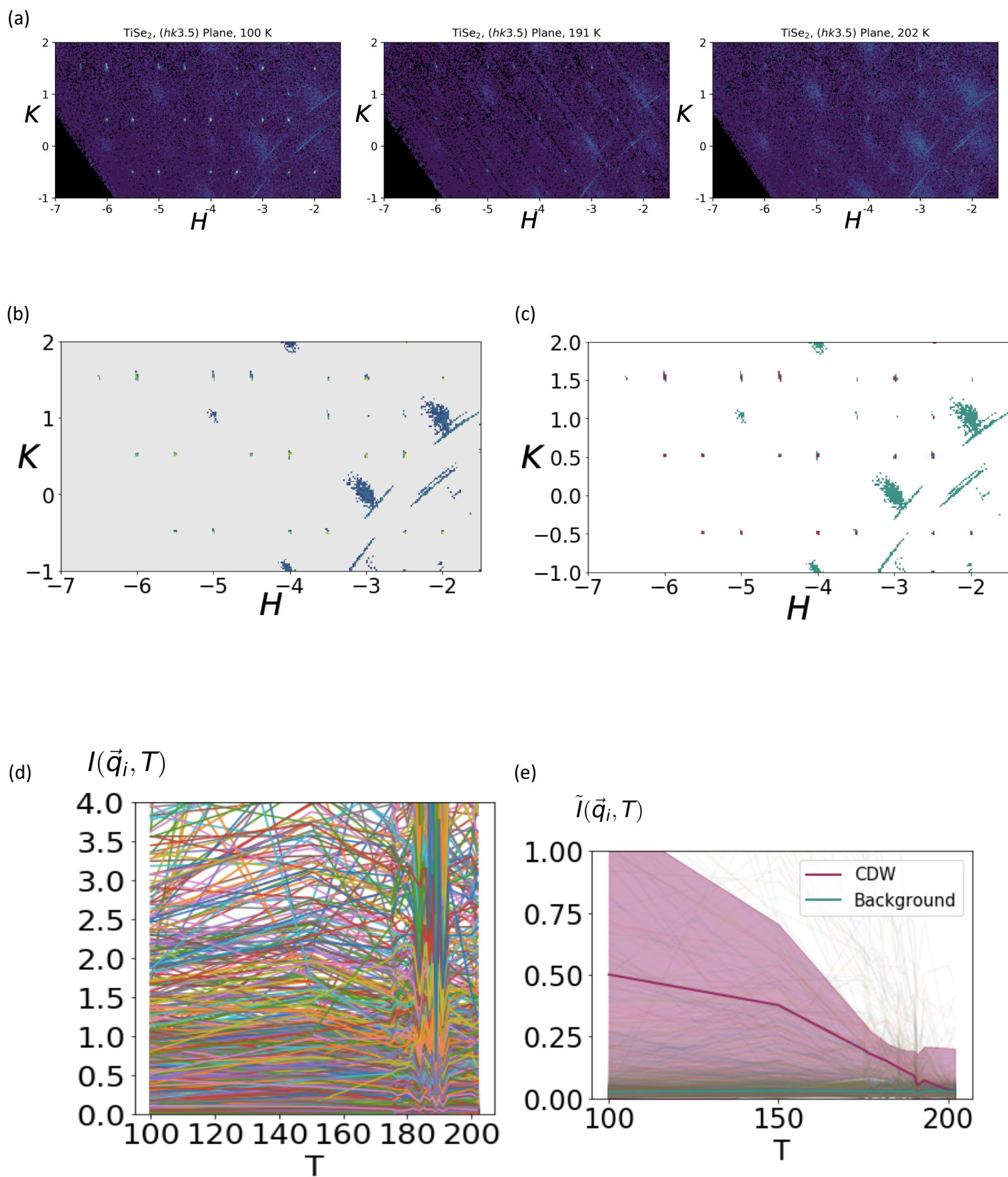


Figure 3

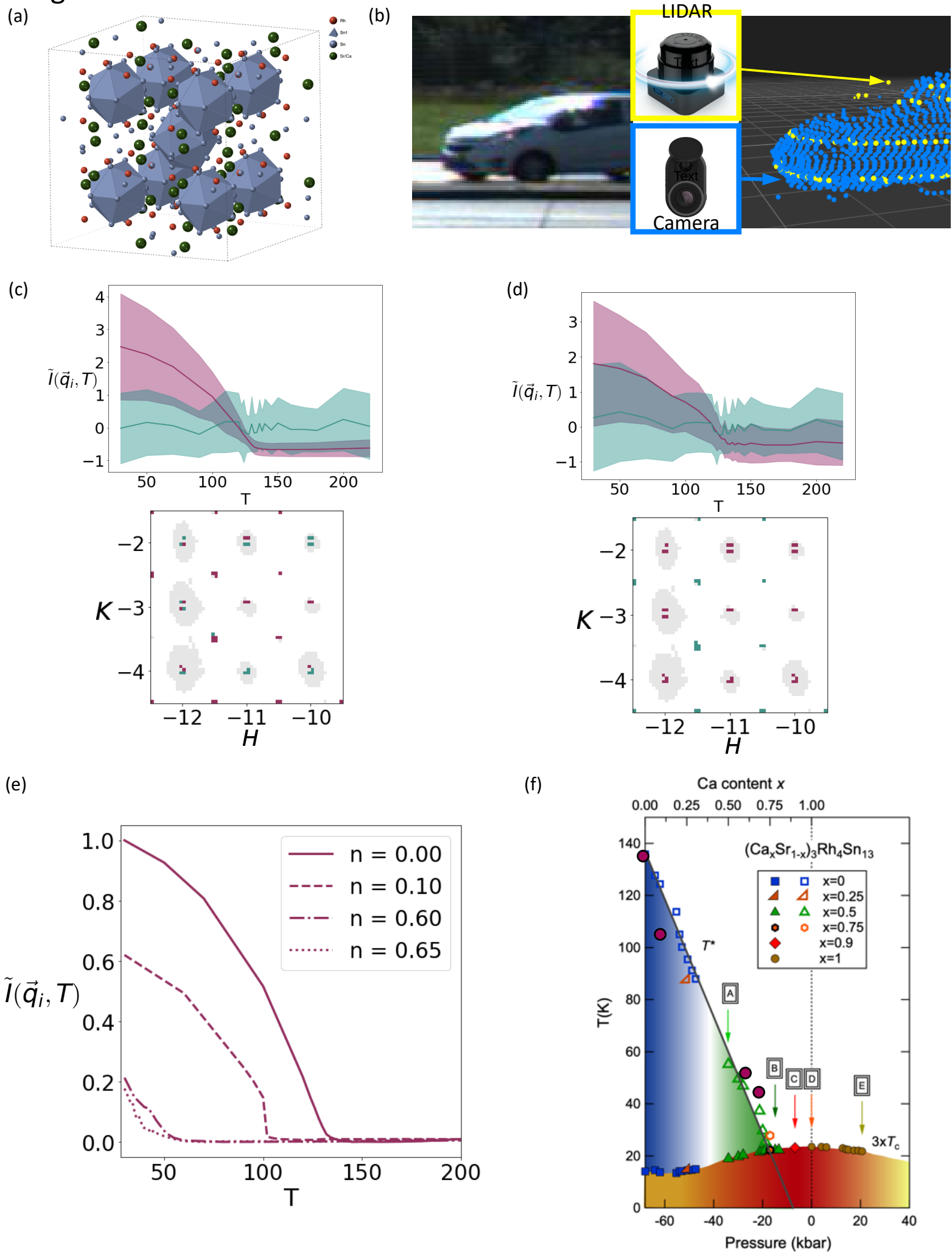
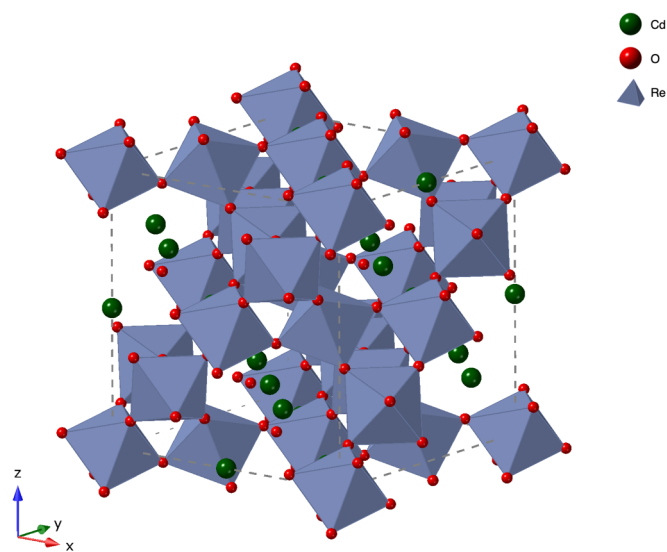
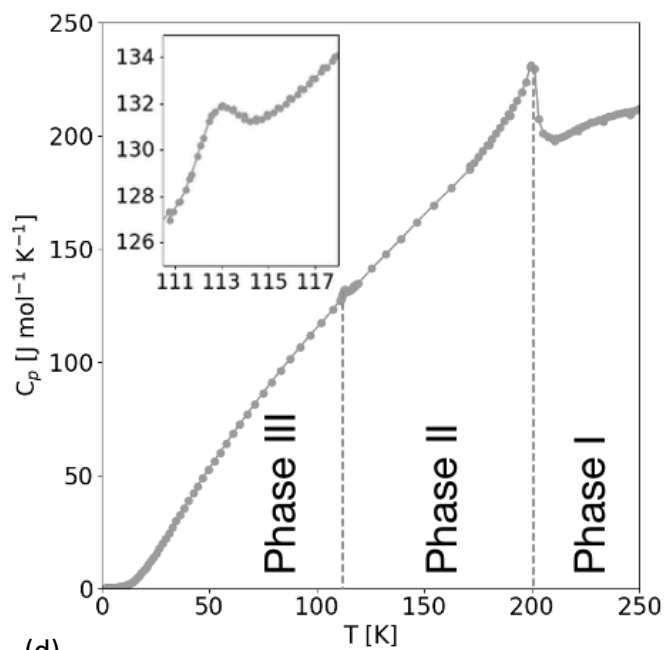


Figure 4

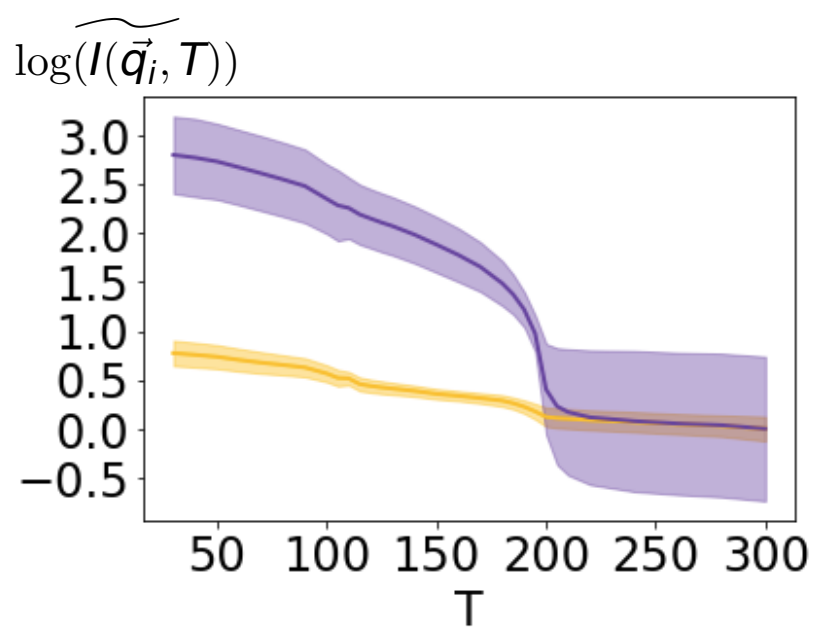
(a)



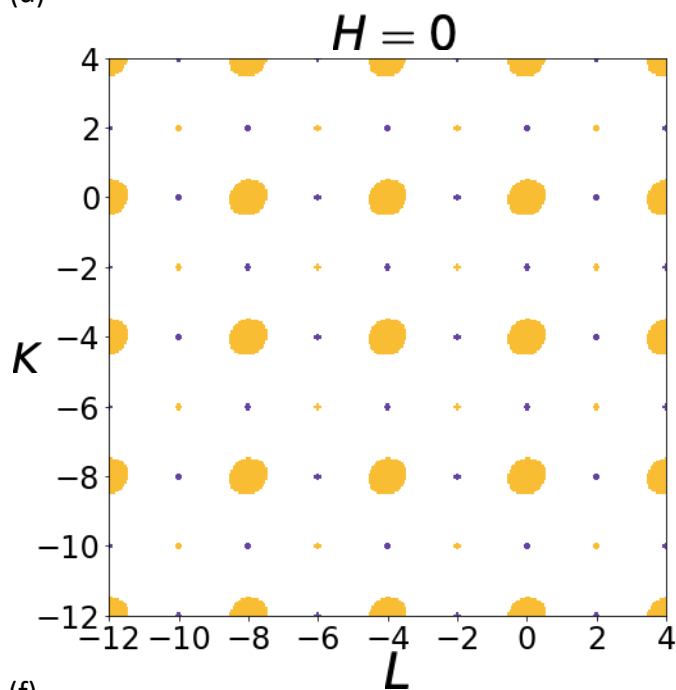
(b)



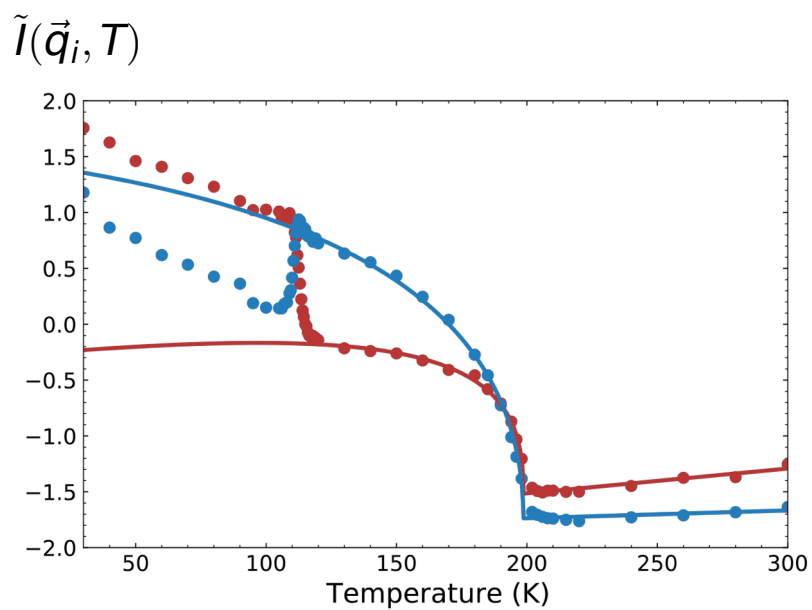
(c)



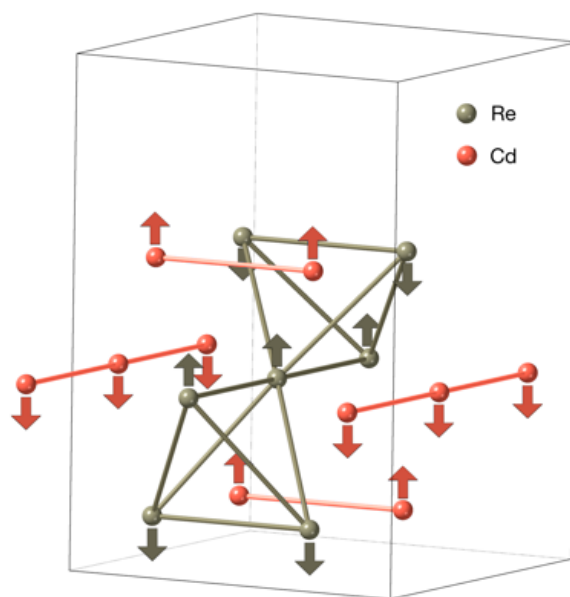
(d)



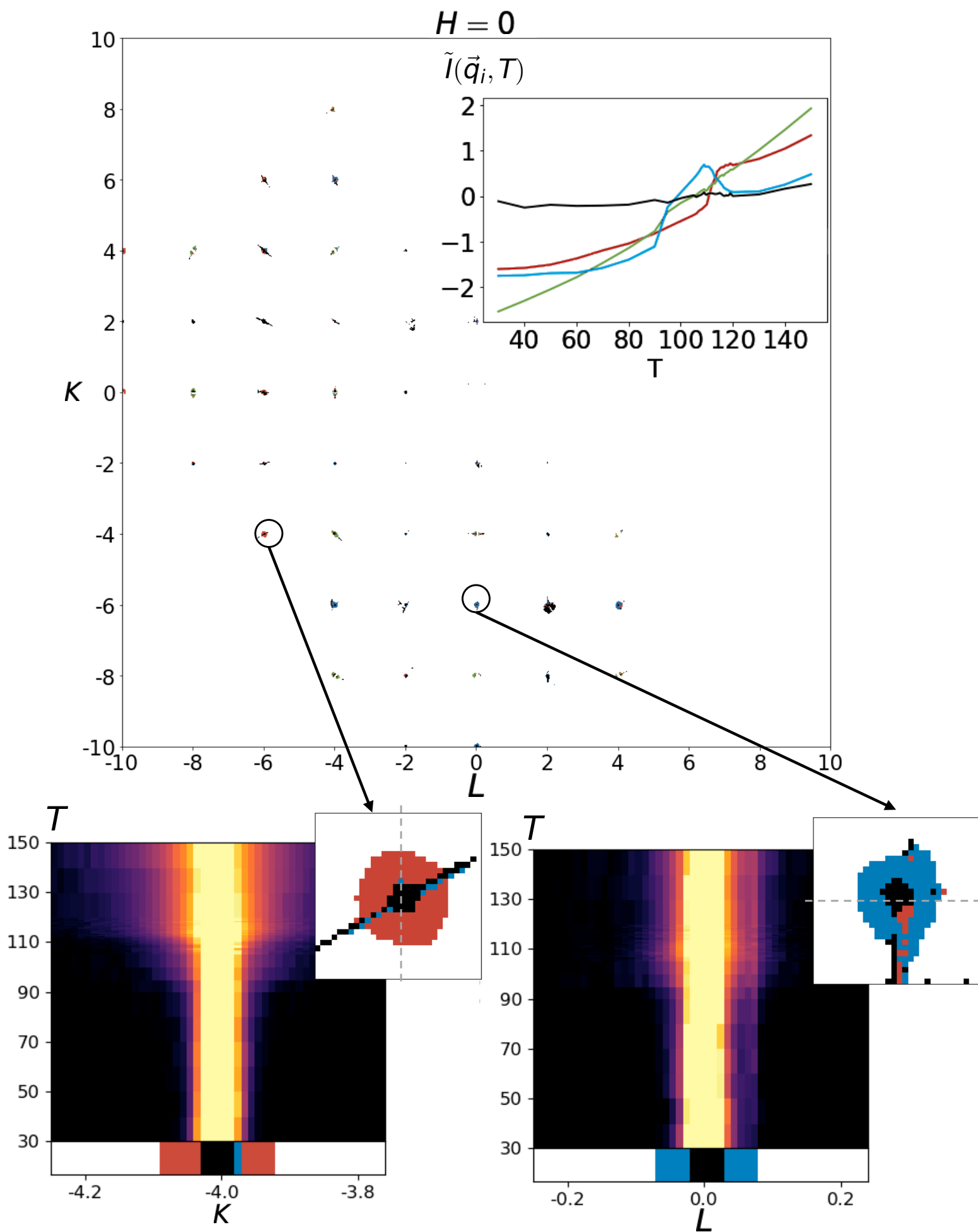
(e)



(f)



(g)



# Harnessing Interpretable and Unsupervised Machine Learning to Address Big Data from Modern X-ray Diffraction

Jordan Venderley<sup>1</sup>, Michael Matty<sup>1</sup>, Matthew Krogstad<sup>2</sup>, Jacob Ruff<sup>3</sup>,  
Geoff Pleiss<sup>4</sup>, Varsha Kishore<sup>4</sup>, David Mandrus<sup>5</sup>, Daniel Phelan<sup>2</sup>,  
Lekh Poudel<sup>6,7</sup>, Andrew Gordon Wilson<sup>8</sup>, Kilian Weinberger<sup>4</sup>,  
Puspa Upreti<sup>2,9</sup>, Stephan Rosenkranz<sup>2</sup>, Raymond Osborn<sup>2</sup>, Eun-Ah Kim<sup>1\*</sup>

<sup>1</sup>Department of Physics, Cornell University

<sup>2</sup>Materials Science Division, Argonne National Laboratory

<sup>3</sup>Cornell High Energy Synchrotron Source, Cornell University

<sup>4</sup>Department of Computer Science, Cornell University

<sup>5</sup>Department of Materials Science and Engineering, University of Tennessee

<sup>6</sup>Department of Materials Science and Engineering, University of Maryland

<sup>7</sup>NIST Center for Neutron Research, National Institute of Standard and Technology

<sup>8</sup>Courant Institute of Mathematical Sciences, New York University

<sup>9</sup>Department of Physics, Northern Illinois University

\*To whom correspondence should be addressed; E-mail: eun-ah.kim@cornell.edu.

(Dated: April 9, 2024)

## SUPPLEMENTARY INFORMATION

### I. X-RAY MEASUREMENTS

A schematic of the x-ray measurement scattering geometry is shown in Fig. 1 of the main article. Three-dimensional volumes of diffuse X-ray scattering were collected at Advanced Photon Source (APS) and CHESS. The APS data were measured on sector 6-ID-D using an incident energy of 87.1 keV and a detector distance of 638 mm, except for the high-resolution measurements on  $\text{Cd}_2\text{Re}_2\text{O}_7$ , which used an incident energy of 60.0 keV and a distance of 1406 mm. The raw images were collected on a Dectris Pilatus 2M with a 1-mm-thick CdTe sensor layer. The data were collected over a temperature range of 30 K to 300 K, with samples cooled by flowing He gas below 105 K and  $\text{N}_2$  gas above 105 K. The CHESS data on  $\text{TiSe}_2$  were measured on beamline A2 using an incident beam energy of 59 keV and a Dectris Pilatus 6M detector with a 1-mm-thick Si sensor layer. The data were collected over a temperature range of 90 K to 300 K, with samples cooled by flowing  $\text{N}_2$  gas. During the measurements, the samples were continuously rotated about an axis perpendicular to the beam at  $1^\circ\text{s}^{-1}$  over  $360^\circ$ , with images read out every 0.1 s. Three sets of rotation images were collected for each sample at each temperature to fill in gaps between the detector chips. The resulting images were stacked into a three-dimensional array, oriented using an automated peak search algorithm and transformed in reciprocal space coordinates using the software package CCTW (Crystal Coordinate Transformation Workflow), allowing  $S(\mathbf{Q})$  to be determined over a range of  $\sim \pm 15 \text{ \AA}^{-1}$  in all directions ( $\sim \pm 6 \text{ \AA}^{-1}$  for the high-resolution measurement on  $\text{Cd}_2\text{Re}_2\text{O}_7$ ). Further details are given in ref. 1.

### II. X-TEC: XRD TEMPERATURE CLUSTERING

#### A. Preprocessing

In this section we describe the technical details of *X-TEC*. A signature difficulty in the analysis of X-ray diffraction data is the existence of physics at several different intensity scales. This is only further exacerbated when probing low-intensity features where the signal-to-noise ratio can be small. If one is to employ thresholding as part of some preprocessing, it is imperative to be careful in order to avoid thresholding-out any important physics. Nevertheless, thresholding is extremely useful for mitigating the influence of noise and for reducing dataset size since most single crystal x-ray diffraction patterns are sparse. Consequently, we propose a new thresholding methodology for isolating the physically relevant regions of k-space.

A naive way to cluster the type of datasets offered by single crystal x-ray diffraction is to apply an i.i.d. assumption and directly try to cluster the associated trajectories,  $I(\vec{q}_i, T)$ , so that each  $q$ -point is classified according to its functional temperature dependence. However, such an attempt is immediately thwarted by the existence of a continuum of trajectories spanning over a large intensity range as seen in fig. 1g so that getting any meaningful clustering is difficult. The standard way of dealing with this is to use feature scaling a.k.a. standardization in which one removes the mean for each trajectory and then normalizes it by dividing by its standard deviation. However, the dominant features of x-ray diffraction data are usually relatively well-localized peaks and most trajectories may be attributed to background fluctuations and thermal diffuse scattering. These trajectories have small, finite means and variances so that conventional standardization amplifies the underlying experimental error and noise, thereby spoiling any immediate attempt at clustering. On the other hand, failing to standardize makes it difficult to cluster over different energy scales since low-intensity variations can be washed out by larger ones. Thus some cutoff is needed in order to avoid clustering over noise while maintaining the ability to cluster over different energy scales.

In order to properly threshold our data, we exploit the statistical properties of our trajectories' average intensities,  $\log \bar{I}(\vec{q}_i, T)$ . Here, the average is performed over temperature so that a single average intensity is obtained for each  $\mathbf{q}$ . Several properties of our data make it advantageous to examine the statistics of  $\log \bar{I}(\vec{q}_i, T)$  rather than  $\bar{I}(\vec{q}_i, T)$ , most notably its positive semi-definiteness and large range. Since the dominant features our data are naturally sparse and the background trajectories are characterized by possessing small means and variances, we should expect the distribution of  $\bar{I}(\vec{q}_i, T)$  to be sharply peaked near some relatively small background value. Looking at the logarithm,  $\log \bar{I}(\vec{q}_i, T)$ , broadens this peak allowing us to resolve the finer structural details of this low-intensity background. To first order, we find the distribution of  $\log \bar{I}(\vec{q}_i, T)$  to be well-characterized by a bulk background contribution that is approximately normally distributed at low intensities with sparsely distributed high intensity contributions. This can be seen in when looking at the distribution of  $\log \bar{I}(\vec{q}_i, T)$  for a single unit-cell of  $\text{TiSe}_2$  in fig. S1. In order to separate these high intensity features from rest of the data, we take advantage of their sparsity relative to the background. Specifically, we minimize the Kullback-Leibler divergence  $D_{KL}$ , where for probability distributions  $p(x), q(x)$ :

$$D_{KL}(p(x)||q(x)) = \sum_{x \in X} p(x) \ln \frac{p(x)}{q(x)} \quad (1)$$

between the distribution of  $\log(\overline{I(\vec{q}_i, T)})$  with a high intensity cutoff and a gaussian. Information theoretically, the Kullback-Leibler divergence quantifies the information loss associated with approximating the distribution  $p(x)$  by  $q(x)$ . In this context, the minimizing  $D_{KL}$  optimally chooses a high-intensity cutoff so that the distribution of the remaining  $\log \overline{I_q}(T)$  looks closest to a normal distribution. This is illustrated by applying our procedure to a single unit-cell of  $\text{TiSe}_2$  in Fig. S1. Optimization is performed via gradient descent. Note that optimizing with this sliding cutoff is necessary and a Gaussian cannot be directly fitted because the distribution  $\log \overline{I(\vec{q}_i, T)}$  is heavy tailed. Directly fitting with a Gaussian yields a higher cutoff susceptible to missing important low-intensity features.

After thresholding, we find it convenient for the  $(\text{Ca}_x\text{Sr}_{1-x})_3\text{Rh}_4\text{Sn}_{13}$  data to rescale by dividing by the mean and subtracting one. This has the advantage over z-scoring of allowing us to implement another thresholding step in which we only cluster over high variance trajectories. In particular, it bolsters the model's ability to cluster distinct functional behaviors together because clusters can no longer be smoothly connected to the origin. However, in the case of the  $\text{TiSe}_2$ , we found it sufficient to simply subtract the mean.

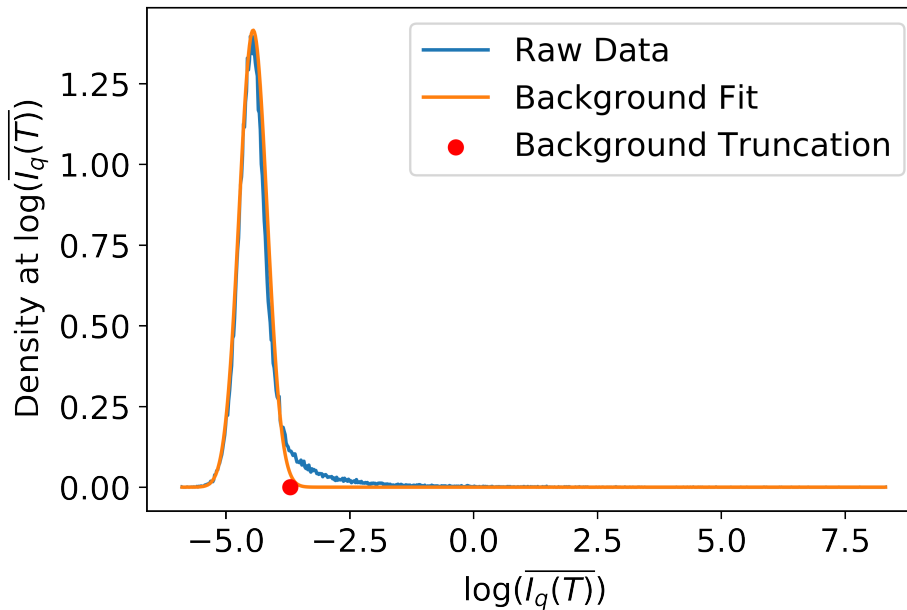


FIG. S1. Histogram (blue) of  $\log \overline{I(\vec{q}_i, T)}$  for a single unit-cell of  $\text{TiSe}_2$  with background fit (orange) and truncation point described in the main text.

For large volumes of data, the average local intensity scale can change substantially for Brillouin zones far from  $\mathbf{q} = 0$  so that any global thresholding method will over-threshold in some regions and under-threshold in others. This may be circumvented by independently thresholding local regions. However, local thresholding can result in instabilities if one tries to threshold regions lacking sufficient statistics, such as zones lying on the boundary of where data was collected. It is also possible, although rare, for the KL-optimization to get stuck at a local maxima that doesn't correspond to the background peak. This is especially problematic when thresholding over tens of thousands of Brillouin zones where the thresholding can't be checked by hand. We are currently in the process of making this thresholding process more sophisticated by using machinery such as Gaussian processes and random forests to infer a continuous thresholding scheme based on the local thresholds. Such a scheme would be capable of identifying potential mistakes in thresholding and provide appropriate thresholds for boundary regions. This will yield a smoother, more robust thresholding scheme.

## B. Label Smoothing

While the vanilla GMM algorithm is able to effectively identify the CDW phase transition, it nevertheless possesses some undesirable properties, most notably it employs an i.i.d. assumption between momenta. Clearly, this assumption is not true since the intensities of nearby momenta are correlated, as are the intensities associated with different unit cells. Exploiting these correlations should result in a more robust algorithm. Here we incorporate label smoothing as a first order approach for incorporating these correlations by allowing labels to diffuse between neighboring points and between unit cells. It ultimately results in cleaner, smoother classifications that better align with intuition.

Typical label smoothing is a semi-supervised method in which there exists a ground truth for certain points. These labelings are then “clamped” and diffused through the rest of the system. Here, we lack a bona fide ground truth and so instead incorporate label smoothing dynamically in between the E and M steps of our EM algorithm. Physically, this adds a diffusive “force” to our update scheme that encourages a similar labeling of nearby points and points differing by a reciprocal lattice vector. Convergence in this modified EM method occurs when an equilibrium is reached between this diffusion and the GMM clustering.

Our label smoothing requires us to construct a weighted graph connecting similar momenta in order for diffusion to occur. This may be done by computing the following kernel:

$$K(k, k') = \exp \left[ - \sum_i \sin^2 \left( \frac{Q_i}{2} \cdot (k - k') \right) / \ell^2 \right] \quad (2)$$

where the  $Q_i$  are the reciprocal basis vectors and  $\ell$  is the relevant length scale for the local correlations. The structure of this kernel is shown in Fig. S2 where  $K(k, 0)$  is plotted as an intensity for a 2D slice.

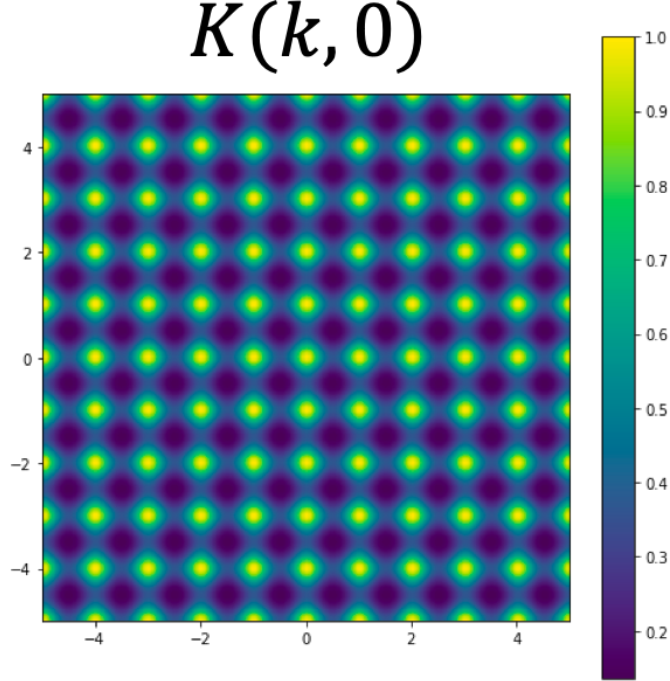


FIG. S2. Kernel,  $K(k, 0)$ , showing the similarity between the origin and momenta in a 2D.

This kernel is really just a weighted adjacency matrix. By incorporating a cutoff in the weights, we may exploit the sparsity of our system for fast matrix-vector multiplication. When handling large datasets, this cutoff is essential since the full kernel is too large to be stored in any reasonable amount of RAM. Define  $A$  to be the matrix associated with this kernel after having normalized the rows i.e. it is row stochastic so that  $\sum_j A_{ij} = 1$ . Now define  $P$  to be the matrix consisting of cluster probabilities calculated by the E-step. Specifically, let the first index correspond to the different momenta and the second to the cluster probabilities so that  $P$  is also row stochastic. Then the product  $AP$  is also

row stochastic since  $\sum_{jk} A_{ij} P_{jk} = \sum_j A_{ij} (1) = 1$ . So by multiplying  $P$  by  $A$ , we generate a new set of diffused cluster probabilities. The strength of this diffusion can be controlled by the number of matrix multiplications. However, note that we cannot simply apply  $A$  until  $A^n P$  converges, because the largest eigenvector of  $A$  is just the constant vector. In practice, we find that even a single application of  $A$  between E- and M-steps is sufficient for obtaining smooth labelings. Results are shown for  $(\text{Ca}_x\text{Sr}_{1-x})_3\text{Rh}_4\text{Sn}_{13}$  below.

### C. Derivation of EM algorithm for GMM and general proof of convergence.

We follow derivations in Refs. 2 and 3. First recall Jensen's inequality: for convex function  $f$  and random variable  $X$ ,  $\mathbb{E}[f(X)] \geq f(\mathbb{E}[X])$  where for strictly convex functions, equality holds iff  $X = \mathbb{E}[X]$  almost surely. Let  $\ell(\theta)$ , denote the model log-likelihood and  $X$  be our dataset with  $x_i \in X$ . Then

$$\begin{aligned} \ell(\theta) &= \log p(X; \theta) = \sum_i \log p(x_i; \theta) = \sum_i \log \sum_{z_i} p(x_i, z_i; \theta) \\ &= \sum_i \log \sum_{z_i} q_i(z_i) \frac{p(x_i, z_i; \theta)}{q_i(z_i)} \geq \sum_{i, z_i} q_i(z_i) \log \frac{p(x_i, z_i; \theta)}{q_i(z_i)} \equiv \tilde{\ell}(q, \theta) \end{aligned} \quad (3)$$

where  $q_i(z_i)$  is some distribution over a random variable  $z_i$  (in our case this will be the cluster assignment) s.t.  $\sum_{z_i} q_i(z_i) = 1$  and we have used Jensen's inequality. In order for this bound to be tight,  $X = \mathbb{E}[X] \implies q_i(z_i) = p(z_i|x_i; \theta)$ . Tightness of this bound implies that improving  $\tilde{\ell}(q, \theta)$  necessarily improves  $\ell(\theta)$  but since  $\theta$  is unknown, we will have to make a guess,  $\theta_t$ , and improve it iteratively. This iterative prescription is known as expectation maximization (EM). It consists of an E-step, where  $q_i^t \leftarrow p(z_i|x_i; \theta_t)$  and an M-step  $\theta^{t+1} \leftarrow \underset{\theta}{\operatorname{argmax}} \tilde{\ell}(q^t, \theta)$ .

We now derive the EM algorithm for the GMM. The E-step follows directly from the model likelihood and Bayes' theorem:

$$\begin{aligned} w_i^k &\equiv p(z_i = k|x_i; \pi_k, \mu_k, \Sigma_k) = \frac{\pi_k \mathcal{N}(x_i|\mu_k, \Sigma_k)}{\sum_k \pi_k \mathcal{N}(x_i|\mu_k, \Sigma_k)} \\ \mathcal{N}(x_i|\mu_k, \Sigma_k) &\equiv \frac{1}{(2\pi)^{n/2}} \frac{1}{\sqrt{\det \Sigma_k}} e^{-\frac{1}{2}(x_i - \mu_k)^\dagger \Sigma_k^{-1} (x_i - \mu_k)} \end{aligned} \quad (4)$$

For the M-step, we must find  $\{\pi, \mu, \Sigma\}$  that optimizes our lower log-likelihood bound:

$$\tilde{\ell}(\{w_i^k, \pi_k, \mu_k, \Sigma_k\}) = \sum_{i,k} w_i^k \log \left[ \frac{\pi_k \mathcal{N}(x_i|\mu_k, \Sigma_k)}{w_i^k} \right] + \lambda (1 - \sum_k \pi_k) \quad (5)$$

where  $\lambda$  is a Lagrange multiplier constraining the mixing weights to sum to unity.

Solving for the mixing weights:

$$\begin{aligned} 0 &= \partial_{\pi_j} \tilde{\ell} = \sum_{i,k} w_i^k \frac{1}{\pi_k} \delta_{jk} - \lambda \sum_k \delta_{jk} \implies \lambda = \frac{1}{\pi_j} \sum_i w_i^j \\ \lambda &= \lambda \sum_k \pi_k = \sum_{i,k} w_i^k = \sum_i 1 \equiv m \\ \implies \pi_j &= \frac{1}{m} \sum_i w_i^j \end{aligned} \quad (6)$$

Solving for the mean:

$$\begin{aligned} 0 &= \partial_{\mu_l} \tilde{\ell} = 2 \sum_i w_i^l \Sigma_l^{-1} (x_i - \mu_l) \\ \implies \mu_l &= \frac{1}{\sum_i w_i^l} \sum_i w_i^l x_i \end{aligned} \quad (7)$$

Solving for the covariance is a little trickier. First note the following matrix identities for symmetric invertible matrix  $A$ :

$$\begin{aligned}\partial(\log(\det A)) &= \text{Tr}(A^{-1}\partial A) \\ \partial A^{-1} &= -A^{-1}(\partial A)A^{-1}\end{aligned}\tag{8}$$

Now, when solving for the covariance we promote the covariance cluster index to an upper index so that the lower indices refer to the matrix elements:

$$\begin{aligned}0 &= \partial_{\Sigma_{mn}^l} \tilde{\ell} = \sum_{i,k} w_i^l \partial_{\Sigma_{mn}^l} \left[ \log \det \Sigma^k + (x_i - \mu_k)^\dagger (\Sigma^k)^{-1} (x_i - \mu_k) \right] \\ &= \sum_{i,k} w_i^l \left[ \delta_{lk} \text{Tr} \{ (\Sigma^{k-1})_{rs} \delta_{sm} \delta_{tn} \} - \delta_{lk} \sum_{ps} (x_i - \mu_k)_p^\dagger \left\{ \sum_{qr} (\Sigma^{k-1})_{pq} \delta_{mq} \delta_{nr} (\Sigma^{k-1})_{rs} \right\} (x_i - \mu_k)_s \right] \\ &= \sum_i w_i^l \left[ \Sigma_{nm}^{l-1} - \sum_{p,s} (x_i - \mu_l)_p^\dagger \Sigma_{pm}^{l-1} \Sigma_{ns}^{l-1} (x_i - \mu_l)_s \right] \\ &= \sum_i w_i^l \left[ \Sigma^{l-1} - \Sigma^{l-1} (x_i - \mu_l) (x_i - \mu_l)^\dagger \Sigma^{l-1} \right] \\ 0 &= \sum_i w_i^l \left[ \Sigma^l - (x_i - \mu_l) (x_i - \mu_l)^\dagger \right] \\ \implies \Sigma_l &= \frac{1}{\sum_i w_i^l} \sum_i w_i^l (x_i - \mu_l) (x_i - \mu_l)^\dagger\end{aligned}\tag{9}$$

Note that all quantities derived about have the same form as one would expect from standard regression but with each data point  $x_i$  having a cluster weight  $w_i^k$ .

### III. $\text{Cd}_2\text{Re}_2\text{O}_7$ ANALYSIS

#### A. Specific Heat Measurements

In the main text, the heat capacity ( $C_p$ ) of  $\text{Cd}_2\text{Re}_2\text{O}_7$  was displayed in Fig. 4b. The data shown in that figure was processed by a standard method in relaxation calorimetry (pseudostatic method) in which the heat capacity is assumed to be constant throughout the heating and cooling segments of an applied heat pulse during which  $\Delta T \ll T$ . However, in the presence of a 1st order transition, the shape and magnitude of a peak in  $C_p$  at the phase transition temperature can be modified, while the hysteresis can be lost, when using the pseudostatic method. For this reason, we have also used the scanning method for which  $C_p$  is numerically determined at every point in the warming and cooling segments, which yields a more accurate peakshape and hysteresis for a 1st order transition at the cost of noise and absolute accuracy. A more detailed description of pseudostatic and scanning analysis can be found in Ref. 4. Fig. S3 shows the temperature dependence of  $C_p$  in the vicinity of the  $\sim 113$  K phase transition when analyzed using the scanning method. A small but resolvable thermal hysteresis was observed between the peaks in  $C_p$  from the heating and cooling curves, which is suggestive of a latent heat and hence a first-order character. We do note, however, that the peak height and width of the peak in  $C_p$  did not differ substantially between these two methods, as would also be anticipated for a first-order transition, and for this reason the analysis of  $C_p$  alone is not definitive in identifying the order of the transition.

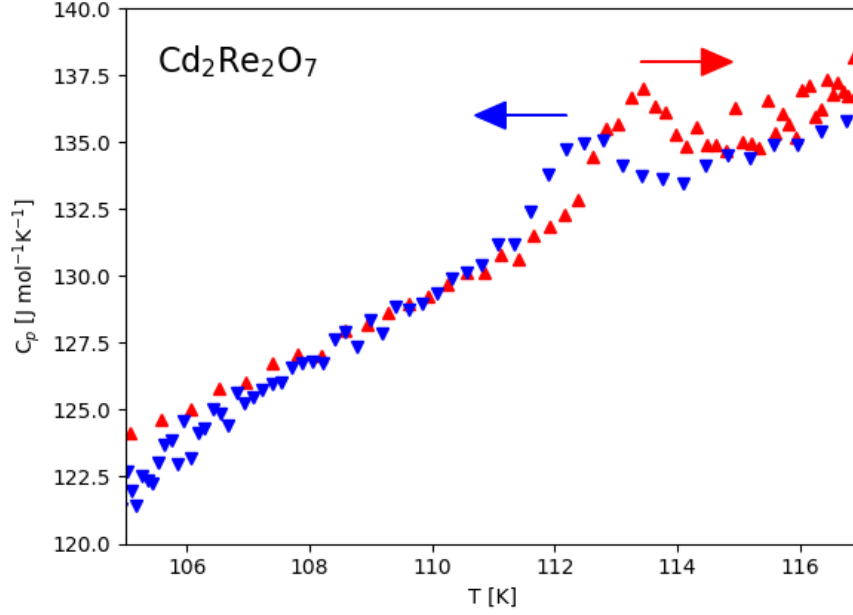


FIG. S3. Specific heat of  $\text{Cd}_2\text{Re}_2\text{O}_7$ , measured using the scanning method described in the text.

### B. Preprocessing and clustering setup details

Here we specify different preprocessing steps and clustering choices for the analysis of  $\text{Cd}_2\text{Re}_2\text{O}_7$  data presented in Fig. 4.

- **Fig 4c - peak-averaged, low resolution data.**

1. In order to reduce noise, we first construct an average BZ mask by thresholding every BZ as described in II(a) and then averaging the thresholded BZs together.
2. We then manually select a cutoff value for the averaged BZ that maintains all the peaks while removing as much background as possible, and set each  $\vec{q}$ -point in the average BZ with value greater than the cutoff to 1, and the rest to 0 to form the mask.
3. We multiply each BZ by the average BZ mask to remove noise and emphasize the peaks.
4. Beginning from the known peak centers, we floodfill to pick out all  $\vec{q}$ -points belonging to each peak.
5. We perform peak averaging by averaging the trajectories of all  $\vec{q}$ -points belonging to each peak and replacing them with the single, averaged trajectory.
6. We rescale the data by taking the log of one plus each peak-averaged trajectory, and subsequently subtracting the mean.
7. Finally we cluster using  $K = 2$  clusters. We subtract the minimum value of the cluster means when plotting to emphasize the order-parameter like behavior of the purple cluster in fig. 4d.

- **Fig 4e - peak averaged, high resolution data.**

1. We begin by selecting a  $50 \times 50 \times 50$  region around each known peak center and thresholding as described in SM II(a).
2. We then floodfill from the peak centers and average all resulting trajectories to form a single, averaged trajectory per peak.
3. We rescale the data by z-scoring it.

4. We cluster the peak-averaged trajectories using  $K = 4$  clusters. We found four clusters to be the minimum number necessary to separate all distinct behaviors and that there was no advantage to using more than four.
5. In fig. 4(e), the dotted lines show the two clusters that exhibit order parameter-like behavior.

• **Fig 4g - peaks opened, high resolution data.**

1. We select a  $50 \times 50 \times 50$  window around each known peak center and threshold as described in SM II(a).
2. We only include the  $H$  layers of peaks that we know are potentially interesting from a symmetry breaking perspective. This is every other layer of the extended BZ.
3. We rescale the data by z-scoring it.
4. We cluster the data using  $K = 4$  clusters. The resulting cluster means are shown in the inset in figure 4(g).

### C. Structure Factor Analysis

Fig. S4 shows the cluster means for all four clusters identified by peak-averaged machine learning, including two already shown in Fig. 4e of the main article. It should be noted that these clusters represent the average temperature dependence of all the peaks assigned to their respective clusters, so there can be large variations within each cluster. However, the ML analysis has identified distinctive behavior in each cluster that we have verified by manual inspection of a number of peaks. All four clusters show similar temperature dependence close to the transition at  $T_{s1} = 200$  K, but strikingly different behavior at the lower transition at  $T_{s2} = 113$  K. The blue cluster peaks show a sudden drop in intensity while the red cluster peaks show a sudden increase. The green and orange cluster peaks show a sharp spike in intensity at  $T_{s2}$ , before falling back to their values just above the transition. We do not currently have an explanation for this remarkable behavior.

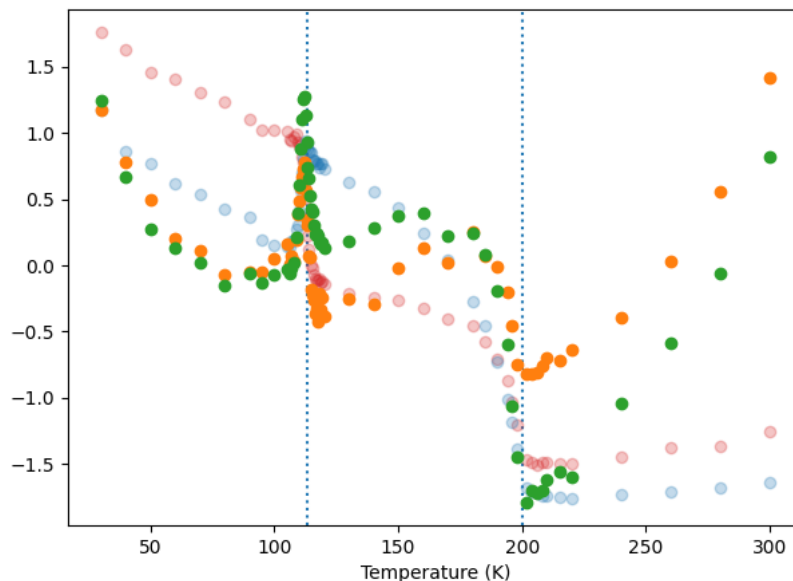


FIG. S4. Four-cluster  $X$ -TEC results on the high resolution measurements on  $\text{Cd}_2\text{Re}_2\text{O}_7$ . Two of these sub-clusters are shown in Fig. 4e (red and blue points, faded for clarity). The other two sub-clusters (green and orange points) arise from peaks that are not forbidden in the high-temperature cubic phase. The temperatures of the two structural phase transitions are shown as dotted lines.

The structural phase transition at  $T_{s1}$  is from the cubic pyrochlore structure, with space group  $Fd\bar{3}m$ , to a distorted tetragonal structure, with space group  $I\bar{4}m2$ . This space group allows distortions of the cadmium and rhenium cations along the  $z$  direction and either the  $x$  or  $y$  direction depending on the Wyckoff positions, using the  $I\bar{4}m2$  unit cell,

which is rotated by  $45^\circ$  from the cubic unit cell, *i.e.*,  $x$  is parallel to the (110) direction of the high-temperature cubic structure. There are associated displacements of the oxygen ions, but the x-ray measurements are not sensitive to them.

Analytic calculations of the structure factors for the Bragg peaks in terms of the allowed  $x$  and  $z$  distortions fall into four groups that correspond well to the four ML clusters. For example, the two groups whose intensities are forbidden in the high-temperature cubic phase (red and blue) have the following form:

$$F_1(H, K, L) \propto (-1)^{n_3} \sum_{M=\text{Cd,Re}} \{f_M [(-1)^{n_1} \cos(2\pi H \delta x_M) e^{-2\pi L \delta z_M} + (-1)^{n_2} \cos(2\pi K \delta x_M) e^{2\pi L \delta z_M}]\} \quad (10)$$

where  $n_1 = \frac{1}{2}H$ ,  $n_2 = \frac{1}{2}K$ , and  $n_3 = \frac{1}{4}(L - 2)$ .

$$F_2(H, K, L) \propto (-1)^{n_3} \sum_{M=\text{Cd,Re}} \{f_M [(-1)^{n_1} \sin(2\pi H \delta x_M) e^{-2\pi L \delta z_M} + (-1)^{n_2} \sin(2\pi K \delta x_M) e^{2\pi L \delta z_M}]\} \quad (11)$$

where  $n_1 = \frac{1}{2}(H - 1)$ ,  $n_2 = \frac{1}{2}(K - 1)$ , and  $n_3 = \frac{1}{4}L$ .

It can be seen that, for small values of  $H$  and  $K$ ,  $F_1(H, K, L)$  are mostly sensitive to distortions along the  $z$ -axis, whereas for small values of  $L$ ,  $F_2(H, K, L)$  is mostly sensitive to in-plane distortions along  $x$  or  $y$  (where  $\delta x = \delta y$ ). The assignments of individual peaks in the *X-TEC* analysis show that the (H,K,L) values of the blue cluster are indeed dominated by in-plane distortions whereas the red cluster peaks are dominated by  $z$ -axis distortions. This suggests that the distinctive temperature dependences of peaks in the blue and red clusters can be used to derive information about the relative distortions along  $x$  and  $z$ . If we assume that the temperature dependence of  $\delta x$  and  $\delta z$  follows that expected for an order parameter with a common critical exponent,  $\beta$ , from 200 K down to 120 K, the peak intensities would vary as  $(T - T_c)^{2\beta}$ .

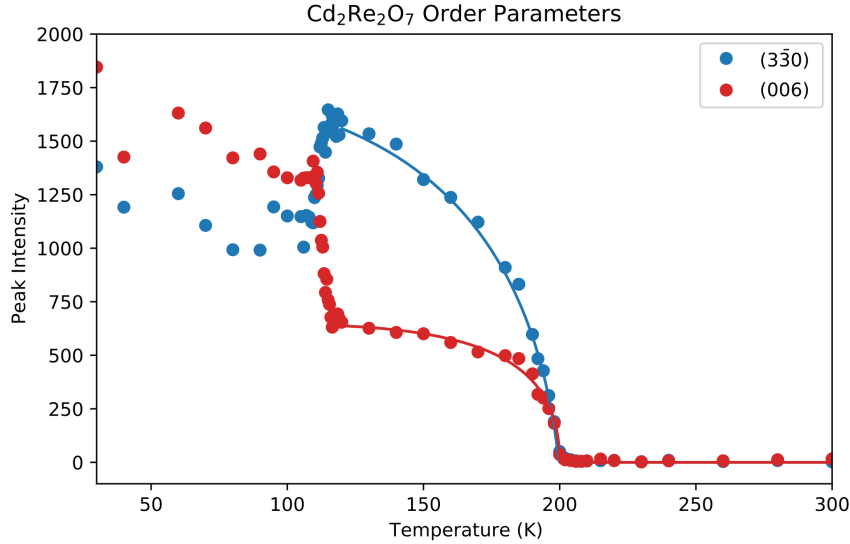


FIG. S5. Temperature dependence of the 006 and  $3\bar{3}0$  Bragg peaks (blue and red circles, respectively). These correspond to the  $00\bar{6}$  and  $0\bar{6}0$  peaks using the indices of the high-temperature cubic phase. The blue and red solid lines are fits between 120 K and 300 K to the structure factors in equations 10 and 11, respectively, assuming that the distortions,  $\delta x$  and  $\delta z$  for the Cd and Re ions, vary as  $(T - T_c)^\beta$ , with  $\beta = 0.25$  and  $T_c = 200$  K.

As an example, Figure S5 compares the 006 and  $3\bar{3}0$  peaks, which correspond to the  $00\bar{6}$  and  $0\bar{6}0$  peaks in the cubic phase. These are peaks that have been assigned to the two sub-clusters shown in Fig. 4e. Equations 10 and 11 show that the 006 peak is only sensitive to  $\delta z_{\text{Cd}}$  and  $\delta z_{\text{Re}}$ , whereas the  $3\bar{3}$  peak is only sensitive to in-plane distortions. The fit to the 006 peak yields relative  $z$ -axis distortions that are equal and opposite, *i.e.*,  $\delta z_{\text{Re}} = -\delta z_{\text{Cd}}$ , illustrated in Fig. 4f. The out-of-phase distortions are the reason for the flattening of the peak intensity of the 006 peak between 180 K and 120 K, confirming the conclusions based on the fits to the cluster means in Fig. 4e. On the other hand, the  $3\bar{3}0$  peak follows the scaling law from 200 K to 120 K, showing either that  $\delta x_{\text{Re}}$  has the same sign as  $\delta x_{\text{Cd}}$  or that one of the distortions is much larger than the other. This is an example where the temperature dependence of the peak intensities below a structural phase transition yields information on the relative internal distortions, which have proved to be too subtle for conventional crystallographic refinement until now.

### D. Temperature Dependence of Diffuse Scattering

Fig. 4g in the main article showed four-cluster ( $K=4$ ) assignments of the high-resolution data allowing each q-point to behave independently. This reveals differences between clusters in the diffuse scattering halo around the Bragg peaks, which represent fluctuations in the order parameter at the  $\Gamma$  point. Peaks in the blue cluster, which are also assigned to the blue cluster in Fig. S5, display weak diffuse scattering halos in the range  $T_{s2} < T < T_{s1}$  while peaks in the red cluster displayed much stronger diffuse scattering halos in this region, as seen in Fig. 4g. This is clearly illustrated in Fig. S6, where the temperature dependence of the diffuse scattering in the blue and red clusters are compared. Both show strong critical scattering at  $T_{s1}$ , but the diffuse contribution is much stronger in peaks assigned to the red cluster, which are most sensitive to the out-of-phase  $z$ -axis fluctuations of the Re and Cd sublattices. We attribute these strong  $z$ -axis fluctuations to the Goldstone modes seen in Raman scattering<sup>5</sup>, which are fluctuations between the two nearly degenerate  $E_u$  modes. This interpretation is justified by the fact that the Goldstone modes are fluctuations from the  $I4m2$  ground state to  $I4_122$  symmetry, in which  $\delta z$  is constrained to be 0. It is therefore not surprising that  $z$ -axis fluctuations are dominant.

The  $X$ -TEC clusters shown in the inset to Fig. 4g were derived from data below 150 K. The blue cluster shows a substantial increase in diffuse scattering just above  $T_{s2}$ , whereas the red cluster shows a weaker peak just above  $T_{s2}$ . Since the trajectories shown in the inset to Fig. 4g are shown with respect to their mean value, the absolute difference in the diffuse scattering intensity above  $T_{s2}$  is not as clear in Fig. 4g as in Fig. S6.

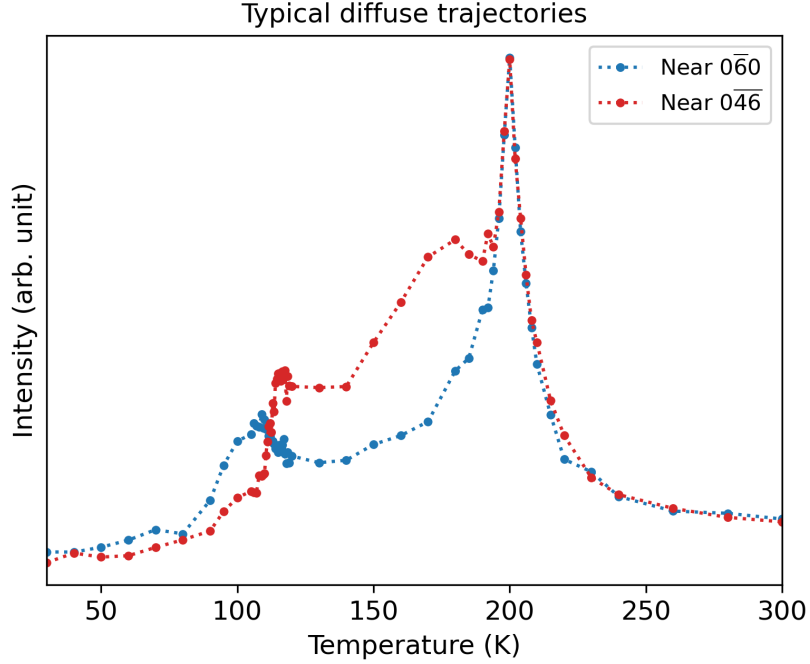


FIG. S6. Temperature dependence of the diffuse scattering near the  $0\bar{6}0$  and  $0\bar{4}6$  Bragg peaks shown in Fig. 4g (blue and red circles, respectively). The temperature dependence of each is taken at a representative point offset from the central Bragg peak.

<sup>1</sup> M. J. Krogstad, *et al.*, *Nature Materials* **19**, 63 (2020).

<sup>2</sup> A. Ng, *CS229 Lecture notes* (2017).

<sup>3</sup> K. P. Murphy, *Machine learning : a probabilistic perspective* (MIT Press, Cambridge, Mass. [u.a.], 2013).

<sup>4</sup> T. M. Gillard, D. Phelan, C. Leighton, F. S. Bates, *Macromolecules* **48**, 4733 (2015).

<sup>5</sup> C. A. Kendziora, *et al.*, *Phys. Rev. Lett.* **95**, 125503 (2005).